



# HHS Public Access

Author manuscript

*Nat Biotechnol.* Author manuscript; available in PMC 2022 June 25.

Published in final edited form as:

*Nat Biotechnol.* 2022 June ; 40(6): 906–920. doi:10.1038/s41587-021-01155-4.

## A humanized mouse model of chronic COVID-19

**Esen Sefik**<sup>1</sup>,  
**Benjamin Israelow**<sup>1,2</sup>,  
**Haris Mirza**<sup>1,4</sup>,  
**Jun Zhao**<sup>1,4</sup>,  
**Rihao Qu**<sup>1,4</sup>,  
**Eleanna Kaffe**<sup>1</sup>,  
**Eric Song**<sup>1</sup>,  
**Stephanie Halene**<sup>3</sup>,  
**Eric Meffre**<sup>1</sup>,  
**Yuval Kluger**<sup>4</sup>,  
**Michel Nussenzweig**<sup>5</sup>,  
**Craig B. Wilen**<sup>1,6</sup>,  
**Akiko Iwasaki**<sup>1,7</sup>,  
**Richard A. Flavell**<sup>1,7</sup>

<sup>1</sup>Department of Immunobiology, Yale University School of Medicine, New Haven, CT

<sup>2</sup>Department of Medicine, Section of Infectious Diseases, Yale University School of Medicine, New Haven, CT, USA

<sup>3</sup>Section of Hematology, Yale Cancer Center and Department of Internal Medicine, Yale University School of Medicine, New Haven, CT

<sup>4</sup>Department of Pathology, Yale University School of Medicine, New Haven, CT, USA.

<sup>5</sup>Laboratory of Molecular Immunology, The Rockefeller University, New York, NY, USA.

<sup>6</sup>Department of Laboratory Medicine, Yale University School of Medicine, New Haven, CT, USA.

<sup>7</sup>Howard Hughes Medical Institute, Yale University School of Medicine, New Haven, CT, USA.

### Abstract

COVID-19 is an infectious disease; in some it presents as an uncontrolled, hyperactive immune response, causing severe immunological injury. Existing rodent models do not recapitulate the sustained immunopathology of patients with severe disease. Here, we describe a humanized mouse model of COVID-19 that uses adeno-associated virus to deliver human ACE2 to the lungs of humanized MISTRG6 mice. This model recapitulates innate and adaptive human immune

---

Users may view, print, copy, and download text and data-mine the content in such documents, for the purposes of academic research, subject always to the full Conditions of use: <https://www.springernature.com/gp/open-research/policies/accepted-manuscript-terms>

Competing financial interests

RAF is an advisor to Glaxo Smith Kline and Zai Lab.

responses to SARS-CoV-2 infection up to 28 days post-infection, with key features of chronic COVID-19 including weight loss, persistent viral RNA, lung pathology with fibrosis, a human inflammatory macrophage response, a persistent interferon-stimulated gene signature, and T-cell lymphopenia. We used this to study two therapeutics on immunopathology: patient-derived antibodies and steroids; We found that the same inflammatory macrophages crucial to containing early infection, later drove immunopathology. This model will enable evaluation of COVID-19 disease mechanisms and treatments.

---

## Introduction:

COVID-19, caused by severe acute respiratory syndrome coronavirus 2 (SARS-CoV-2),<sup>1</sup> is a heterogenous disease with few therapeutic options. Although anti-viral immunity mediates viral clearance in mild COVID-19, robust inflammatory cytokines, decreased circulating lymphocytes, dysregulated myeloid and lymphocyte compartments characterize immunopathology in severe COVID-19<sup>2-13</sup>. Accurate model systems are essential to evaluate promising discoveries, but most available rodent and non-human primate models do not reveal the immunopathology seen in patients and are not well-suited to test therapeutics in the context of severe COVID-19 or post-acute sequelae of COVID-19<sup>14-21</sup>.

ACE2 is a SARS-CoV-2 receptor<sup>22-24</sup>. SARS-CoV-2 does not infect standard laboratory mice due to differences between mouse and human ACE2 (hACE2) that limit viral entry<sup>22-26</sup>. Mice with transgenic or transient hACE2 expression can be infected with SARS-CoV-2<sup>14-17,25</sup>. Although acute viral response, transmission, and vaccine efficacy can be tested in these models, they lack severe, chronic disease (Extended Data Fig.1). We hypothesized that a functional human immune system would model innate and adaptive human immunity during SARS-CoV-2 infection and confer chronicity and pathology seen in patients. Mice with a human immune system (humanized mice), generated via transplantation of human hematopoietic stem and progenitor cells (HSPCs), are invaluable tools to study the human immune system *in vivo*<sup>27,28</sup>. MISTRG6<sup>29</sup> mice were engineered by a human/mouse homolog gene-replacement strategy to provide physiological expression with regard to quantity, location and time of **M-CSF** (monocytes and tissue macrophage development)<sup>30</sup>, **GM-CSF/IL-3** (lung alveolar macrophages)<sup>31</sup>, **SIRP $\alpha$**  (macrophage tolerance to human cells)<sup>32</sup>, **ThPO** (hematopoiesis and platelets)<sup>33</sup>, and **IL-6** (improved engraftment and antibody responses)<sup>34-36</sup>, in a **Rag2/Gamma** common chain deleted background. When engrafted with human HSPCs, these mice have a comprehensive immune system comparable to humans<sup>29,37</sup>. Delivering hACE2 via an Adeno-associated virus (AAV)-vector to the lungs<sup>18</sup> allows SARS-CoV-2 infection of HSPC engrafted MISTRG6 mice. Thus, we created a humanized mouse model of COVID-19 that recapitulates the human innate and adaptive immune systems that is amenable to the mechanistic study of COVID-19 and its myriad of complications.

## Results:

### **MISTRG6 humanized mice that transiently express hACE2 can be infected with SARS-CoV-2.**

We delivered AAV-hACE2<sup>18</sup> to the lungs of immune-reconstituted MISTRG6 mice (*MISTRG6-hACE2*) that have been engrafted with human HSPCs (Fig. 1A). *MISTRG6-hACE2* mice were then infected with SARS-CoV-2 which yielded comparable viral RNA levels and viral titers to wild type mice<sup>18</sup> but with prolonged high viral titers and RNA for at least 35 days post-infection (dpi) (Fig. 1B–C, S1A–B). In contrast, MISTRG6 mice lacking AAV-hACE2 expression did not have detectable viral titers, confirming the necessity of hACE2 for infection (Fig. 1C). Of note, *MISTRG6-hACE2* mice that were infected but not engrafted with human HSPCs (and thus lack human immune cells), had lower viral titers than infected mice with human immune cells (Fig. 1C). The presence of human immune cells in *MISTRG6-hACE2* mice caused persistent disease with severe, chronic weight loss for at least 35 dpi (Fig. 1D, S1C). *MISTRG6-hACE2* humanized mice also exhibited more severe lung pathology compared to other animal models<sup>16,18,19,21,38</sup>. This lung pathology followed the three stages described in human COVID-19 patients: exudative, organizing, and fibrotic phases<sup>4,39–42</sup>. At 2dpi, *MISTRG6-hACE2* mice showed prominent collection of proteinaceous debris in the alveolar spaces, hallmarks of the exudative phase (Fig. 1E, S1D). Lungs at 4dpi transitioned into organizing phase, highlighted by infiltration of alveolar spaces by lymphocytes, macrophages, and fibroblasts (Fig. 1E, S1D, 2C). Between 14 and 28dpi, expanding infiltration of interalveolar spaces (Fig. 1E, S1D–F) and increasing deposition of collagen, highlighted by thickening of collagen bundles in the lung parenchyma (Fig. 1F, S1D–F), further obliterated alveolar architecture. These changes highlighted the transition from the organizing to fibrotic phase. The architectural remodeling and collagen deposition was more pronounced at 28 and 35dpi resulting in replacement of normal alveolar architecture by dilated cystic spaces, separated by thick interstitial tissue bands (Fig. 1E–F, S1D–F). Thus, these data suggest humanized *MISTRG6-hACE2* mice model chronic disease, and recapitulate the severe, persistent lung pathology seen in patients with severe COVID19.

### **Inflammatory macrophages and monocytes characterize the Immune landscape in SARS-CoV-2 infected MISTRG6-hACE2 mice.**

We next characterized human and mouse immune cells in SARS-CoV-2 infected and uninfected *MISTRG6-hACE2* mice by flow cytometry to evaluate the cells that drive immunopathology and viral clearance (Fig. S2A–B). The degree of humanization was comparable in blood between uninfected and infected mice, but SARS-CoV-2 infection drastically increased recruitment of human immune cells to the lower respiratory tract and lung parenchyma, as quantified in whole lung homogenates and bronchioalveolar lavage (BAL) (Fig. 2A–B). The infiltrates present in lungs and BAL at 2–4 dpi consisted of human monocytes, macrophages, and T cells (Fig. 2C), again reminiscent of human COVID-19 lung pathology<sup>7</sup>. In our model, human neutrophils are lacking so instead we measured mouse neutrophils, the most abundant mouse immune cells in these mice (Fig. S2B). In contrast to persistent human immune cell infiltration, mouse immune cell and neutrophil infiltration was transient, peaking at 4dpi and returning to baseline by 14dpi (Fig. S2B).

Variability in neutrophils is in line with human histopathological findings in lungs<sup>43</sup>. Yet, the cause of such variability and whether this is a result of superimposed bacterial infections is unestablished<sup>44,45</sup>.

The lung monocytes of infected mice comprised all three human monocyte subsets (CD14+ classical; CD14+CD16+ intermediate; and CD16+ non-classical; Fig. 2C). By contrast, and in line with healthy human lung monocytes<sup>46</sup>; uninfected humanized mouse lungs harbored only classical CD14+ monocytes which expanded in response to SARS-CoV-2 infection (Fig. 2C). Intermediate and non-classical monocytes infiltrated infected lungs at high frequencies as early as 2dpi, peaking at 4dpi. Macrophage numbers increased at 4dpi, and peaked at 14dpi, remaining high until 28dpi (Fig. 2C, D, S2C,D). By 2dpi, the macrophage compartment was enriched for inflammatory and monocyte-derived macrophages, which outnumbered alveolar macrophages, suggesting macrophages recruited early from the circulation are the long-term contributors of immunopathology (Fig. 2E–G). Plasmacytoid dendritic cells (pDCs), generally known for their contribution to early antiviral response and main producers of type I interferon alpha (IFN $\alpha$ ), were enriched substantially later in infection (14dpi in Fig. 2H). Infected mice at 14dpi also showed activated pDCs (Fig. 2I, S2E) marked by CCR7 and CD83 expression<sup>47</sup>. This coincided with chronically sustained interferon response and sustained inflammatory macrophages, as seen in severe COVID-19 patients<sup>7,8,48,49</sup>.

### **Adaptive immune responses of COVID-19 patients are recapitulated in MISTRG6-hACE2 mice infected with SARS-CoV-2.**

Human COVID-19 shows profound T cell lymphopenia<sup>10,12,16,50</sup> that is recapitulated in our humanized mice. Infected *MISTRG6-hACE2* humanized mice presented with a profound loss of T cells, especially CD8+ T cells, in blood and spleens (Fig. 3A–B, Extended Data Fig. 2A–C). Moreover, lung T cells of *MISTRG6-hACE2* mice were activated (positive for HLA-DR, CXCR3, ICOS and PD1) and the main producers of IFN-gamma (IFN $\gamma$ ) (Fig. 3C–D, 4B,D) as in COVID-19 patients<sup>10–12</sup>. T cell populations comprised both TCRalpha/beta T cells (T $\alpha\beta$ ), enriched for CD4+, and TCRgamma/delta T cells (T $\gamma\delta$ ) in both uninfected and infected mice (Fig. 3E, Extended data Fig.2D). Yet, during the course of infection, as the circulating T cell numbers decline, the total number of T cells in lungs increased with higher representation of T $\gamma\delta$  cells compared with uninfected mice (Fig. 3E). The early T cell response in infected lungs showed an increase in resident and infiltrating T $\gamma\delta$  cells and bystander activated memory T $\alpha\beta$  cells as determined by the lung transcriptional profile (Fig. 4C, Extended Data Fig.4H).

As the human cells in these mice develop within a mouse thymus, we wished to determine whether T cells were responsive to virus in the context of MHC developed in our system. To test this, we stained human CD8+ T cells from infected mice that had been engrafted with an HLA-A2 positive source of HSPCs with viral antigen-bearing HLA-A2 tetramers (Extended data Fig.2E). Virus specific CD8+T $\alpha\beta$  cells against membrane glycoprotein (M) and Spike (S) peptides were detectable as early as 4dpi, peaking at 28dpi (Fig 3F). To test if these T cells could attenuate infection, we transferred sorted lung T cells and total splenocytes from infected mice to unengrafted *MISTRG6-hACE2* mice prior to infection with SARS-CoV-2.

Viral titers at 4dpi in mice which received prophylactic lung T cells were clearly lower than mice which did not receive human T cells (Extended data Fig.2F). Thus, a functional anti-SARS-CoV-2 T-cell response develops in infected *MISTRG6-hACE2* mice.

B cells gradually increased in response to infection, peaking late at 14–28dpi in BAL and lungs (Fig. 3G, Extended data Fig.2G). Although the germinal center B cell response was reported to be suboptimal in reconstituted *MISTRG6* mice<sup>35</sup>, a high proportion of IgM+ B cells were seen early in infection that were subsequently replaced by IgG+ B cells (14dpi and 28dpi) and thus defined the anti-viral B cell response (Fig. 3H–I, Extended data Fig.2H). B cells, particularly late in infection, expressed high levels of CD11c (Fig 3J, Extended data Fig.2I), implicating an inflammatory, systemic lupus erythematosus (SLE)-like extrafollicular B cell response<sup>51,52</sup> in humanized COVID-19, reminiscent of the human disease<sup>53</sup>. In contrast to T cell lymphopenia, B cell numbers in the humanized mice were normal or even increased (Fig 3G, Extended data Fig.2J) as in the majority of patients<sup>54</sup>. A robust memory B-cell expansion is detected early in human infection with serum IgM and IgA antibodies detected earlier than IgG<sup>30</sup>. Initial serum IgM and IgA titers in human SARS-CoV-2 infection decline (~28 days), as IgG titers peak (~49 days)<sup>55</sup>. We observed a similar dynamic for IgM+ and IgG+ B cells in humanized lungs with IgM+ B cells declining over time and IgG+ B cells emerging at 14dpi and reaching high levels at 28dpi, at which point serum IgG levels also peak (Fig. 3H, I, Extended data Fig.2H,K). Thus, *MISTRG6-hACE2* humanized mice recapitulate T and B cell responses induced by SARS-CoV-2 infection in patients.

**SARS-CoV-2 lungs sustain ISGs and display SLE-like features.**—We evaluated the transcriptional landscape in uninfected and SARS-CoV-2 infected lungs of humanized mice at 2, 4, 7, 14, and 28dpi. Mapping of transcripts to the human genome or the mouse genome separately identified 285 human genes and 516 mouse genes that were over-represented in infected lungs (Fig. 4A, Table S1). This approach served as a proxy for identifying changes in human vs mouse immune cells. Although there was marked heterogeneity in the strength of the response, the anti-viral response was sustained throughout the course of infection, suggesting that early anti-viral responses were either maintained or amplified late in infection (Fig. 4A). Corresponding pathway analysis of these differentially expressed mouse genes (mouse DEGs) identified cellular responses to interferons, cytokine production, ribonuclease activity, and neutrophil activation as top biological processes induced during SARS-CoV-2 infection (Table S2). Human DEGs were enriched for extracellular matrix assembly, opsonization, complement activation with a focus on immune phenotypes in monocytes, activated T cells and B cells; this further corroborated our findings from flow cytometric analysis (Table S2). Similar circuitries of monocytes, macrophages, activated T cells and extrafollicular B cells were described in humans with SARS-CoV-2 pneumonia<sup>53,56</sup>.

We performed single cell RNA sequencing to better evaluate the phenotype of human and mouse cells in lungs of infected *MISTRG6-hACE2* mice. Our transcriptome analysis of human cells at the single cell level also revealed that human macrophages, monocytes, and human T cells were abundant at 4dpi (Fig. 4B–C). Human monocytes infiltrating infected lungs were already differentiating into macrophages at this stage of infection.

These infiltrating monocytes and macrophages (clusters 0,1,2,3) were the main producers of inflammatory cytokines IL-1A, IL-1B, TNF and IL-6, like in severe COVID-19 patients<sup>6,9–11,13</sup>, (Fig. 4B,D). As in recent studies characterizing human COVID-19<sup>56</sup>, alveolar macrophages in infected *MISTRG6-hACE2* mice were the main producers of T cell chemoattractants such as CXCL10 (Fig. 4D). We also monitored mouse immune cells, predominantly enriched for neutrophils (clusters 1,2) few mouse monocytes (clusters 5,6) and macrophages (cluster 3) at 4dpi (Extended Data Fig.3A,B). Mouse neutrophils which peak at 4dpi (Fig. S2B) were the main producers of mouse inflammatory cytokines and chemokines (*Il1a*, *Il1b*, *Tnf*, *Il18*, *Cxcl10*; Extended Data Fig.3C).

Notably, the majority of the human and mouse DEGs in lungs were type-I or type-II interferon stimulated genes (ISGs) (Fig. 4E, Table S1–3). ISGs were sustained at high levels throughout infection persisting even as late as 14dpi and 28dpi, recapitulating the interferon-dependent phenotypes identified in COVID-19 patients (Fig. 4A,E; Table S2, 3)<sup>13,48,49,57</sup>. Despite their fundamental role in many infectious and inflammatory diseases, the direct quantitation of type-I interferons has been challenging in health and disease<sup>58</sup>. Despite a significant ISG signature, minimal amounts of type-I interferons have been detected in the blood or lungs of patients with severe COVID-19<sup>59–62</sup>. This contrasts with that seen in patients infected with highly pathogenic influenza viruses<sup>63</sup>. We first quantified type-I interferons by qPCR. Of the many IFNA gene transcripts we tested (IFNA1, IFNA2, IFNA6, IFNA8, IFNA14, and IFNA21), only IFNA1 and IFNA6 mRNA levels were reliably detected and increased upon infection with SARS-CoV-2, peaking at 14dpi and coincident with pDC numbers in the lung tissue (Fig. 4F). We observed a similar but not significant trend for IFNB levels (Extended Data Fig.3D). Next, we quantified IFN $\alpha$  levels by ELISA in infected and uninfected mice. IFN $\alpha$  levels in serum and BAL, although low, mirrored transcript levels primarily produced by lung pDCs (Extended Data Fig.3E–F). Interferons during the recovery phase of influenza infection have been shown to prevent epithelial cell proliferation and differentiation, hence interfering with lung repair<sup>64</sup>. Likewise, our findings suggest that sustained type-I interferon signaling may also contribute to persistent lung pathology in COVID-19, as supported by histopathological assessment of 14–28 dpi lungs, when interferon levels are particularly high (Fig. 1E,F, Table S3). Human and mouse DEGs were also enriched for type-II ISGs (Fig. 4E). Type-II interferon, IFN $\gamma$ , was mainly produced by T cells (Fig. 4D) as early as 2dpi and sustained until 28dpi. (Fig. 4G, Extended Data Fig.3G). In addition, elevated levels of various pro-inflammatory cytokines and chemokines (IL6, IL8, TNF, IL1B, CXCL10, IFNG) peaked or remained high late in infection further supporting delayed immune-resolution (Fig. 4G). An inflammatory cytokine signature (particularly IL6<sup>6,10</sup> and IL8<sup>65</sup>), recapitulated in our model, was closely correlated with COVID-19 severity in patients<sup>6,66</sup>. Elevated serum TNF- $\alpha$  levels were not as predictive of severity as other cytokines (IL6<sup>6,10</sup>, IL8<sup>65</sup>) in patients, but correlated with viral load<sup>6,10</sup>. TNF- $\alpha$  levels in *MISTRG6-hACE2* mice were also higher early in infection with a similar but weaker correlation (Pearson's  $r=0.25$ ) between TNF- $\alpha$  and viral N transcript, suggesting a more pronounced role for TNF- $\alpha$  during the acute phase of disease.

Given the role of type-I interferons on bystander activation of T and B cells<sup>67,68</sup>, we first focused on the genes that typify bystander activation of memory T cells<sup>67</sup>. This suggested that early in infection (2–4dpi), T cell activation may be an antigen-independent,

interferon-driven response (Extended Data Fig.3H). We sought to identify the origin of genes upregulated in patients by validating their expression in our infected mice and then identifying their cellular source<sup>69</sup>. B cell response in humanized lungs was particularly enriched for genes that are upregulated in moderate and severe COVID-19 patients (Extended Data Fig.3I,J). Lack of germinal center formation coupled with extrafollicular B cell responses correlated with poor clinical outcomes in COVID-19 patients<sup>53,70</sup>. In line with these observations, unbiased pathway analysis of the 28dpi lung transcriptome (Fig. 4A, Extended Data Fig.3I, Table S2) and a more focused look at the SLE gene signatures<sup>71</sup> identified a particular enrichment of SLE-like extrafollicular responses in lungs of infected mice at 28dpi (Fig. 4H). Furthermore, B cell responses at 28dpi exhibited the features of activated, bystander, clonal B cells that are not vaccine-specific in the context of influenza vaccine response, previously characterized in humans<sup>68</sup> (Extended Data Fig.3K), further suggesting a highly inflammatory, bystander B cell response in humanized COVID-19<sup>10,11,53,69</sup>. Taken together, our lung transcriptome analysis identifies a central role of monocyte derived-macrophage interferon response that persists and is amplified later in infection and suggests that interferons regulate both the innate and adaptive immune response in COVID-19.

### **Human monoclonal recombinant antibodies as prophylactic and therapeutic interventions impact disease outcome.**

We tested whether *MISTRG6-hACE2* mice could be used to evaluate patient-derived human antibodies as modulators of infection. *MISTRG6-hACE2* mice were treated with convalescent plasma<sup>72</sup> before infection with SARS-CoV-2 (Extended Data Fig.4A). The treated mice had significantly lower viral titers in lungs at 4dpi showing the plasma was partially effective (Fig. 5A). Yet, prophylactic convalescent plasma did not prevent weight loss or histopathological transition into the organizing phase, highlighted by immune cell infiltration, particularly inflammatory macrophages, into the alveolar spaces (Fig. 5B–C, Extended Data Fig. 4B,C) These findings highlight the limited efficacy of prophylactic administration of convalescent plasma in controlling lung pathology<sup>73–75</sup>. Monoclonal recombinant antibodies (mAbs) cloned from these convalescent patients had high neutralizing activity against SARS-CoV-2 *in vitro* and *in vivo*<sup>72,76</sup>. Thus, we tested two complementary mAb clones *in vivo* for prophylactic and therapeutic treatments of SARS-CoV-2 infection in humanized mice (Extended Data Fig.4A,I). Mice were either treated with individual mAbs prior to infection, or with both mAbs combined at two time points post-infection (11- or 35-hours post-infection (hpi)) and analyzed at 4dpi (Extended Data Fig.5A,I). As measured by viral titers and viral RNA in lungs, prophylactic treatment with mAbs prevented SARS-CoV-2 infection (Fig. 5D). Prophylactic antibody administration also attenuated immune infiltration, yielding fewer infiltrating immune cells, particularly macrophages in lungs and BAL (Fig. 5E–H, Extended Data Fig.5D). Although T cell activation in lungs was comparable, possibly due to bystander activation of T cells, treatment with mAb clone-144 reduced infiltrating T $\gamma$  $\delta$  cells in lungs (Extended Data Fig.4E, F), and prevented both systemic T cell lymphopenia (Extended Data Fig.4G,H) and weight loss (Fig. 5I). Next, we tested therapeutic mAb treatment in *MISTRG6-hACE2* mice. While therapeutic treatment with mAbs similarly prompted viral clearance at both early and late time points, this failed to prevent immune infiltration or significantly alter

the composition of the immune infiltrate in lungs by contrast to prophylaxis (Fig. 5J–N, Extended Data Fig. 4J,L,M). Humanized mice treated with both mAbs early (11hpi) had fewer immune cells in BAL at 4dpi compared to untreated and late (35hpi)-treated groups, suggesting the inflammatory responses is attenuated by early but less so by late treatment with mAbs (Fig. 5L). Although neither therapeutic intervention prevented weight loss, early treatment prevented systemic T cell lymphopenia, while later mAb administration had little effect, and a similar infiltration profile as untreated mice at 4dpi (Fig 5N, Extended Data Fig. 4K–M). These findings highlight efficacy of mAb treatment in controlling viral infection and viral titers but underline the need for early treatment to control immunopathology, as noted clinically<sup>73–75</sup>

**Accurate timing of corticosteroids is necessary to balance viral clearance and prevent immunopathology.**—Our transcriptome analysis revealed glucocorticoids

as possible upstream regulators of DEGs that are induced in infected lungs (Fig 4A, Table S3). Moreover, given that dexamethasone is thus far the only therapeutic treatment that has strongly impacted recovery and reduced mortality in patients with severe disease<sup>77</sup>, we hypothesized that dexamethasone treatment may attenuate immunopathology in mice infected with SARS-CoV-2. To test this hypothesis, we treated mice with dexamethasone for 3 days starting at 7dpi, when the immune infiltration is established but viral titers had declined in lungs (Extended Data Fig.5A). Mice treated with dexamethasone, recovered weight rapidly by 14dpi and resumed weight gain comparable to their uninfected counterparts (Fig. 6A,1D). Dexamethasone treatment reduced human immune infiltration and reversed immune-activation (Fig. 6B–I). Mouse neutrophils in BAL were fewer in dexamethasone treated mice (Extended Data Fig.5B), and inflammatory macrophages were largely absent from dexamethasone treated mouse lungs (Fig 6C–F). Alveolar macrophages, were restored post-therapy to a frequency similar to uninfected animals (Fig 6E,F). Dexamethasone also blocked accumulation of pDCs (Fig 6G) and reduced T cell activation in lungs (Fig 6H,I and Extended Data Fig.5C). Interestingly, dexamethasone treatment also blocked IgG but not IgM specific B cell responses (Extended Data Fig.5D–E). It was notable that lack of immune cells in dexamethasone treated lungs also correlated with lower viral RNA levels by 28dpi (Extended Data Fig.5F). As the immune infiltrate is established early (by 4dpi), we investigated the timing of dexamethasone mediated control of immunopathology for COVID-19. We treated mice early with dexamethasone for 3 days starting at 3dpi once the immune infiltration was established and viral titers were still high (Extended Data Fig.5G). In stark contrast to late treatment, early dexamethasone treated mice became moribund by 7dpi with rapidly declining weights compared with untreated mice (Fig. 6J). Dexamethasone-treated mice had significantly fewer immune cells infiltrating the lungs and lacked inflammatory macrophages (Fig. 6K, Extended Data Fig.5H). Notably, the disabled antiviral response in these mice led to significantly higher viral loads in the lungs (Fig. 6L). These deleterious consequences of early dexamethasone treatment highlight the importance of the early antiviral response to contain the viral infection. Careful exploration of differential timing of dexamethasone treatment distinguishes the early protective anti-viral response and the subsequent pathological immune response.



## Discussion:

Here, we present a humanized COVID-19 mouse model that combines vector-based delivery of hACE2 and a comprehensive human immune system that recapitulates both innate and adaptive human immunity during SARS-CoV-2 infection. Our model supports chronic disease and enables characterization of the effects of patient-derived antibodies and identification of the sources of immunopathology, in particular the aberrant macrophage response.

Limitations of our model include significant variability between individual animals and to a lesser degree between cohorts. Many parameters may contribute to variability. While each cohort is engrafted with HSPCs from the same donor, the degree of engraftment varies between individual animals and thus each individual animal tested is unique in its baseline human immune system. Different cohorts are engrafted with cells from different donors; thus, there is genetic variability between different cohorts which can be exploited in the future. In this study, we utilized 11 different donors as sources of HSPCs. Further variability can result from experimental differences with the amount of AAV administration and efficiency of cellular infection. Transcriptome analysis revealed differences between individual animals in the strength of the inflammatory response, which may also explain the variable outcome observed in disease outcome in human SARS-CoV-2 infection<sup>78</sup>. Yet, regardless of such heterogeneity, sustained interferon response, as has been postulated in humans<sup>13,48,49,57</sup>, was a common theme that shaped both early anti-viral innate response and late adaptive immune response in humanized COVID-19.

Sustained viral RNA and gross clinical features including failure to recover body weight and severe lung pathology even at very late time points post-infection, are unique among animal models to our MISTRG6 model, with human immune cells and hACE2 expression, which suggests a potential unique contribution of human immune cells to pathology and/or viral RNA persistence. Human immune cells could produce various factors that may impact infected cells, infection dynamics, or be targets of infection themselves. In human lung autopsies, SARS-CoV-2 genomes have been detected in alveolar macrophages<sup>56</sup> which express ACE2. We also have detected viral RNA in sorted human immune cells (hCD45+), specifically in sorted hCD45+CD11b+ cells, enriched for human macrophages, but it is not clear whether RNA detected here is the result of viral replication or a residue of phagocytosed infected epithelial cells. Viral titers measured using sensitive cell culture systems were detectable throughout the duration of disease in engrafted MISTRG6-hACE2 mice. Although lung sampling of viable virus is largely lacking in humans, a few patients with severe disease had positive SARS-CoV-2 culture beyond the acute 10-day window post-symptom onset<sup>79–86</sup>. Chronic disease manifestations reflected in histopathological abnormalities (significant cellular infiltrates, thickened septa, and collagen deposition) of infected humanized lungs late in infection point to lack of recovery and fibrosis, recapitulating severe human COVID-19 lung pathology. To our knowledge, no other COVID-19 disease model recapitulates the chronic weight loss, sustained high viral RNA and chronic histopathology with pulmonary fibrosis as seen in human patients (Extended Data Fig. 1)<sup>4,14–19,21,25,38,40–42,87</sup>. Nonetheless, chronic, humanized COVID-19 is not a lethal disease, which will stimulate further investigation of variables such as age,

pre-existing health conditions and co-morbidities that contribute to high case fatality rate in humans.

Systemic T cell lymphopenia was another common feature of humanized COVID-19 and human disease<sup>11,12,53</sup>. Systemic, cyclical lymphopenia that follows rapid, strong activation of T cells in the infected lungs suggest that T cells are continuously recruited, activated, and consumed in the lungs of infected *MISTRG6-hACE2* mice. In matched samples, we looked for genes in the lung transcriptome that correlate with spleen T cell frequencies to link systemic lymphopenia to transcriptional changes in lungs. Frequencies of splenic T cells negatively correlated with human expression of genes such as *HIF1A*, *UBAP2L*, *MIF*, *FABP7* (Table S4) suggesting inflammation and stress response in lungs, possibly mediated by lung macrophages, may impact systemic lymphopenia. Genes that correlated with systemic lymphopenia were also enriched for ISGs (30/50 top correlating human genes and 26/50 top correlating mouse genes) and suggest some potential therapeutic targets to improve lymphopenia in patients.

*MISTRG6-hACE2* mice allowed the study of two aspects of the immune response: infectious viral clearance and immunopathology. We first evaluated patient-derived human antibodies to study this separation. Despite efficient viral clearance, as measured by sharply reduced viral titers, and lack of antibody mediated enhancement of disease, mAbs when given late did not help prevent the potentially pathological inflammatory response suggesting the players of immune-pathology such as the inflammatory macrophages are recruited very early in infection. Our preclinical data are similar to the clinical experience of more than 20 SARS-CoV-2 specific monoclonal antibodies currently in different stages of clinical trial testing<sup>73-75</sup>. Results so far also support a reduction in viral load upon mAb treatment<sup>73</sup>. Notably, the antibodies prevent hospitalization and death if administered early. Our model could be particularly useful in evaluating efficacy and timing for these antibodies<sup>75</sup>. When administered in a timely manner mAbs could be particularly useful in protecting uninfected individuals and preventing transmission from an infected person by rapid clearance of infectious virus.

Separating the two aspects of the immune response, infectious viral clearance and immunopathology recapitulated in our model, may prove useful in the control of COVID-19. Patients may benefit from early mAb treatment coupled with dexamethasone later in infection. Our data suggest that glucocorticoids, specifically dexamethasone, (decoded as upstream regulators of the inflammatory gene signature in humanized COVID-19) should be considered only when viral titers are undetectable, suggesting timing is crucial in promoting immune-protection while preventing pathology and highlighting the importance of accurate and frequent viral detection methods. When applied to chronic disease dexamethasone effectively controls immunopathology and reverses COVID-19 morbidity. As expected, dexamethasone treatment has broad effects and reverses many aspects of immune-activation. Yet, non-specific suppression of the immune system using dexamethasone early in infection was catastrophic.

Even in the absence of previously described high risk criteria, there are debilitating effects among certain COVID-19 patient groups. Although socio-economic factors may be

responsible for some or all of these effects, perturbation of the proposed system should allow testing of direct medical effects. Our humanized mouse system can be completely personalized by matching patient HSPCs with antibodies and medical history, allowing testing novel therapeutics to address conflicting reports in pre-clinical models and to predict efficacy in patients.

## Materials and Methods

### Mice

MISTRG6 was generated by the R. Flavell laboratory by combining mice generated by this lab, the laboratory of Markus Manz and Regeneron Pharmaceuticals based on the *Rag2*<sup>-/-</sup> *IL2rg*<sup>-/-</sup>129xBalb/c background supplemented with genes for human M-CSF, IL-3, SIRP $\alpha$ , thrombopoietin, GM-CSF and IL6 knocked into their respective mouse loci<sup>29,88</sup>. MISTRG6 mice are deposited in Jackson Laboratories and made available to academic, non-profit, and governmental institutions under a Yale-Regeneron material transfer agreement (already approved and agreed to by all parties). Instructions on obtaining the material transfer agreement for this mouse strain will be available along with strain information and upon request. Unconstituted MISTRG6 mice were maintained with cycling treatment with enrofloxacin in the drinking water (Baytril, 0.27 mg/ml). CD1 strain of mice acquired from Charles River Laboratories were used for cross-fostering of MISTRG6 pups upon birth to stabilize healthy microbiota. C57Bl/6 strain of mice (available in Jackson Laboratories) were used as controls for infection with SARS-Cov-2. All mice were maintained under specific pathogen free conditions in our animal facilities (either Biosafety Level 1, 2 or 3) under our Animal Studies Committee-approved protocol. Mice were housed in 14-hour light and 10-hour dark cycle maintained at 40–60% humidity and 72 degrees F +/- 2 degrees. All animal experimentations were performed in compliance with Yale Institutional Animal Care and Use Committee protocols. For SARS- CoV-2-infected mice, all procedures were performed in a BSL-3 facility with approval from the Yale Institutional Animal Care and Use Committee and Yale Environmental Health and Safety.

### Transplantation of human CD34+ hematopoietic progenitor cells into mice.

Fetal liver samples were cut in small fragments, treated for 45 min at 37°C with collagenase D (Roche, 200  $\mu$ g/ml), and prepared into a cell suspension. Human CD34+ cells were purified by performing density gradient centrifugation (Lymphocyte Separation Medium, MP Biomedicals), followed by positive immunomagnetic selection with EasySep™ Human CD34 Positive Selection Kit (Stemcell). For intra-hepatic engraftment, newborn 1–3 day-old pups were injected with 20,000 fetal liver CD34+ cells in 20  $\mu$ l of PBS were injected into the liver with a 22-gauge needle (Hamilton Company). All use of human materials was approved by the Yale University Human Investigation Committee.

### AAV-hACE2 administration

AAV9 encoding hACE2 was purchased from Vector Biolabs (AAV9-CMV-hACE2). Animals were anaesthetized using isoflurane. The rostral neck was shaved and disinfected. A 5-mm incision was made, and the trachea was visualized. Using a 32-G insulin syringe, a 50- $\mu$ l injection dose of 10<sup>11</sup> genomic copies per milliliter of AAV-CMV-hACE2 was injected

into the trachea. The incision was closed with 4–0 Vicryl suture and/or 3M Vetbond tissue adhesive. Following administration of analgesic animals were placed in a heated cage until full recovery. Mice were then moved to BSL-3 facilities for acclimation.

### **SARS-CoV-2 infection**

SARS-CoV-2 isolate USA-WA1/2020 was obtained from BEI reagent repository. All infection experiments were performed in a Biosafety Level 3 facility, licensed by the State of Connecticut and Yale University. Mice were anesthetized using 20% vol/vol isoflurane diluted in propylene glycol. Using a pipette, 50  $\mu$ l of SARS-CoV-2 ( $1-3 \times 10^6$  PFU) was delivered intranasally.

### **Therapeutics**

MISTRG6-hACE2 mice received prophylactic treatment of convalescent plasma (5ml/kg) or monoclonal antibodies at 10mg/kg (clone 135 -m135 or clone 144-m144) 8 hours prior to infection. SARS-CoV-2 infected MISTRG6-hACE2 mice received a mixed cocktail of monoclonal antibodies clone 135 (m135) and clone 144(m144) at 20mg/kg at 11 hours post-infection for early treatment and 35 hours post-infection for late treatment. SARS-CoV-2 infected MISTRG6-hACE2 were treated with dexamethasone (Sigma) at 10mg/kg for 3 days starting at 7dpi.

### **Viral titers**

Mice were euthanized in 100% isoflurane. Approximately half of the right lung lobe was placed in a bead homogenizer tube with 1 ml of PBS + 2% FBS. After homogenization, 300  $\mu$ l of this mixture was placed in 1mL Trizol (Invitrogen) for RNA extraction and analysis. Remaining volume of lung homogenates was cleared of debris by centrifugation (3,900 g for 10 min). Infectious titers of SARS-CoV-2 were determined by plaque assay in Vero E6 (standard) or Vero ACE2+TMPRSS2+ (sensitive) cells in DMEM 4% FBS, and 0.6% Avicel RC-581<sup>89</sup>. Plaques were resolved at 48 h after infection by fixing in 10% formaldehyde for 1 hour followed by staining for 1 hour in 0.5% crystal violet in 20% ethanol. Plates were rinsed in water to visualize plaques. Multiple dilutions of lung homogenates were used to quantify Infectious titers (minimum number of plaques that can be quantified per ml of lung homogenate=10).

### **Viral RNA analysis**

RNA was extracted with the RNeasy mini kit (Qiagen) per the manufacturer's protocol. SARS-CoV-2 RNA levels were quantified using the Luna Universal Probe Onestep RT-qPCR kit (New England Biolabs) and US CDC real-time RT-PCR primer/probe sets for 2019-nCoV\_N1. For each sample, 1  $\mu$ g of RNA was used.

### **Histology**

Yale pathology kindly provided assistance with embedding, sectioning of lung tissue. A pulmonary pathologist reviewed the slides blinded and identified immune cell infiltration and other related pathologies.

### Isolation of cells and flow cytometry

All mice were analyzed at approximately 9–11 weeks of age. Single cell suspensions were prepared from blood, spleen BAL and lung. Mice were euthanized with 100% isoflurane. BAL was performed using standard methods with a 22G Catheter (BD). Blood was collected either retro-orbitally or via cardiac puncture following euthanasia. BAL was performed using standard methods with a 22G Catheter (BD)<sup>90</sup>. Lungs were harvested, minced, and incubated in a digestion cocktail containing 1 mg/ml collagenase D (Sigma) and 30 µg/ml Dnase I (Sigma-Aldrich) in RPMI at 37°C for 20 min. Tissue was then filtered through a 70-µm filter. Cells were treated with ammonium- chloride-potassium buffer and resuspended in PBS with 1% FBS. Mononuclear cells were incubated at 4C with human (BD) and mouse (BioxCel, BE0307) Fc block for 10 min. After washing, primary antibody staining was performed at 4C for 20 min. After washing with PBS, cells were fixed using 4% paraformaldehyde. For intracellular staining, cells were washed with BD permeabilization buffer and stained in the same buffer for 45 min at room temperature. Samples were analyzed on an LSR II flow cytometer (BD Biosciences). Data were analyzed using FlowJo software 3.2 and plotted using Prism 9 Version 9.2.0 (283).

### Adoptive T cell transfer

Infected lungs (14dpi) were processed as described before. Cells were stained with antibodies against human CD45, human/mouse CD11B, human CD3 and mouse CD45. Lung T cells (humanCD45+ mouseCD45- CD11B-CD3+ cells) were sorted using BD-Aria Cell Sorter in a Biosafety Level 3 facility. Sorted T cells (10,000) were mixed with total splenocytes (10 million) and injected intravenously to unengrafted MISTRG6-hACE2 mice. These mice were then infected as described before and analyzed at 4dpi.

### Antibodies

Antibodies against the following antigens were used: Mouse antigens: CD45 (Clone: 30-F11), Ly6G (1A8), Ly6C (HK1.4), CD31(MEC13.3), CD326 (G8.8); Human antigens: CD45 (HI30), CD3 (UCHT1), CD14 (HCD14), CD16 (3G8), CD19 (HIB19), CD33 (WM53), CD20 (2H7), CD206 (15–2), CD86 (BU63), CD123(6H6), IGM (MHM-88), IGG(M1310G05) CD163 (GHI/61), CD169(7–239) CD68(Y1/82A), CD11B (M1/70), CD11C (3.9), HLA-DR(LN3), CD183 (G025H7), ICOS(C398.4A), PD1 (A17188B), NKp46 (9E2), CD56(MEM-188), CD4(OKT4), CD8(SK1), TCRGD(B1), CCR7(G043H7), CD83(HB15e). All antibodies were obtained from Biolegend, unless otherwise specified.

Details on antibodies were provided as Antigen(clone)/ Fluorochrome/ Supplier/ Catalogue number/ Concentration. Mouse antigens: CD45 (30-F11) PerCP Biolegend 103130 1:200; CD45 (30-F11) FITC Biolegend 103108 1:200; CD45 (30-F11) Brilliant Violet (BV) 711 Biolegend 103147 1:400; Ly6G (1A8) APC/Cyanine7 Biolegend 127624 1:100; Ly6C (HK1.4) BV605 Biolegend 128036 1:400; CD31(MEC13.3) APC/Cyanine7 Biolegend 102507 1:400; CD326 (G8.8) APC/Cyanine7 Biolegend 118218 1:200

Human antigens: CD45(HI30) BV605 Biolegend 304044 1:100; CD45(HI30) Pacific Blue Biolegend 304029 1:100; CD3(UCHT1) PE Biolegend 300408 1:200; CD14(HCD14) APC/Cyanine7 Biolegend 325620 1:100; CD16(3G8) PerCP Biolegend 302030 1:200;

CD16(3G8) FITC Biologend 302006 1:100; CD19(HIB19) APC/Cyanine7 Biologend 302218 1:100; CD19(HIB19) Alexa Fluor 700 Biologend 302226 1:100; CD33(WM53) APC Biologend 983902 1:100; CD20(2H7) APC/Cyanine7 Biologend 302313 1:100; CD20(2H7) Alexa Fluor 700 Biologend 302322 1:100; CD206(15–2) PE Biologend 321106 1:100; CD206(15–2) APC Biologend 321109 1:100; CD86(BU63) PE/Cyanine7 Biologend 374210 1:100; CD123(6H6) PE Biologend 306006 1:100; IGM(MHM-88) APC Biologend 314510 1:100; IGM(MHM-88) APC/Cyanine7 Biologend 314520 1:100; IGG(M1310G05) APC Biologend 410712 1:100; IGG(M1310G05) APC/Cyanine7 Biologend 410732 1:100; CD169(7–239) APC Biologend 346007 1:100; CD11B(M1/70) BV711 Biologend 101242 1:100; CD11C(3.9) PE/Cyanine7 Biologend 301608 1:200; HLA-DR(LN3) Alexa Fluor 700 Biologend 327014 1:100; HLA-DR(LN3) PerCP Biologend 327020 1:400; HLA-DR(LN3) FITC Biologend 327005 1:100; CD183(G025H7) PE/Cyanine7 Biologend 353720 1:100; ICOS(C398.4A) APC Biologend 313510 1:100; CD279-PD1(A17188B) APC/Cyanine7 Biologend 1:100; CD335-NKp46(9E2) PE/Cyanine7 Biologend 331916 1:100; CD56(MEM-188) APC Biologend 304610 1:100; CD56(MEM-188) Pacific Blue Biologend 304629 1:50; CD4(OKT4) BV711 Biologend 317440 1:100; CD8(SK1) Pacific Blue Biologend 344718 1:100; CD8(SK1) BV421 Biologend 344748 1:200; TCRGD(B1) FITC Biologend 331208 1:100; CD163(GH1/61) APC Biologend 333610 1:100; CD68(Y1/82A) BV421 Biologend 333828 1:200; CD83(HB15) APC Biologend 305311 1:100; CCR7(G043H7) PE/Cyanine7 Biologend 353226 1:100; Convalescent plasma and monoclonal antibodies (clone 135 and 144) were acquired from M. Nussenzweig as has been previously described<sup>72</sup>.

### Bulk whole tissue lung RNA-sequencing

RNA isolated from homogenized lung tissue used for viral RNA analysis was also used for whole tissue transcriptome analysis. Libraries were made with the help of the Yale Center for Genomic Analysis. Briefly, libraries were prepared with an Illumina rRNA depletion kit and sequenced on a NovaSeq. Raw sequencing reads were aligned to the human-mouse combined genome with STAR [citation: <https://doi.org/10.1093/bioinformatics/bts635>], annotated and counted with HTSeq [citation: <https://doi.org/10.1093/bioinformatics/btu638>], normalized using DESeq2 [citation: <https://doi.org/10.1186/s13059-014-0550-8>], and graphed using the Broad Institute Morpheus web tool. Differential expression analysis was also performed with DESeq2. For IFN-stimulated gene identification, <http://www.interferome.org> was used with parameters -In Vivo, -Mus musculus or Homo sapiens -fold change up 2 and down 2. Corresponding pathway analysis of differentially expressed mouse and human genes was achieved using multiple platforms (Gene Ontology (GO), Gene Set Enrichment analysis (GSEA), Ingenuity).

### ELISA

IFN $\alpha$  (Sigma) ELISAs were performed based on manufacturer's instruction using serum and BAL fluid from uninfected and infected mice. In short, Triton X-100 and Rnase A were added to serum and BAL samples at final concentrations of 0.5% and 0.5 mg/ml, respectively, and incubated at room temperature (RT) at least 1 hour before use to reduce risk from any potential virus in serum and BAL. For serum IFN $\alpha$  levels, 20 $\mu$ L of serum and for BAL IFN $\alpha$  levels, 100 $\mu$ L of BAL fluid were used.

### Gene expression:

RNA from whole tissue samples was extracted with the Rneasy mini kit (Qiagen) per the manufacturer's protocol RNA from sorted human immune cells (human CD45+), plasmacytoid dendritic cells (PDCs; CD123<sup>hi</sup> CD11B-), macrophages and monocytes (CD11B+) and rest of human immune cells (CD123-CD11B-CD45+) was extracted using Trizol reagent. Expression was normalized to human ACTB or HPRT1. Individual values and means were plotted. High-Capacity cDNA Reverse Transcription Kit was used to make cDNA. Quantitative reverse transcription PCR (qRT-PCR) was performed using an SYBR FAST universal qPCR kit (KAPA Biosystems). Predesigned KiCqStart primers for IFNA1, IFNA2, IFNA6, IFNA8, IFNA14, IFNA21, IFNB, IFNG, HPRT1, ACE2, *Ace2*, *Hprt1* were purchased from Sigma.

### Single Cell RNA Sequencing 10X Genomics

Single cell suspensions from digested lungs were processed for droplet based scRNA-seq and 10000 cells were encapsulated into droplets using 10X Chromium GEM technology. Libraries were prepared in house using Chromium Next GEM Single Cell 3' Reagent Kits v3.1 (10X Genomics). scRNA-seq libraries were sequenced using Nova-Seq. Raw sequencing reads were processed with Cell Ranger 3.1.0 using a human-mouse combined reference to generate a gene cell count matrix. To distinguish human and mouse cells, we counted the number of human genes (nHuman) and mouse genes (nMouse) with nonzero expression in each cell, and selected cells with  $nHuman > 20 * nMouse$  as human cells. The count matrix of human cells and human genes was used in the downstream analysis with Seurat 3.2<sup>91</sup>. Specifically, this matrix was filtered retaining cells with  $> 200$  and  $< 5,000$  genes and  $< 20\%$  mitochondria transcripts. We then log transformed each entry of the matrix by computing  $\log(CPM/100 + 1)$ , where CPM stands for counts per million. To visualize the cell subpopulations in two dimensions, we applied principal component analysis followed by t-SNE, a nonlinear dimension reduction method, to the log-transformed data. Graph-based clustering was then used to generate clusters that were overlaid on the t-SNE coordinates to investigate cell subpopulations. Marker genes for each cluster of cells were identified using the Wilcoxon test with Seurat. For the adjusted P values the Bonferroni correction was used.

### Statistical Analysis

Unpaired or paired t-test was used to determine statistical significance for changes in immune cell frequencies and numbers while comparing infected mice to uninfected control mice. For experiments where mice were treated with monoclonal antibodies or steroids, one-way ANOVA was used to determine statistical significance across groups and adjusted p value was reported. To determine whether the viral RNA quantification is statistically significant across treatment groups or time points, Mann-Whitney, two-tailed test was used. A one-sample Wilcoxon signed rank test was used as a non-parametric alternative to the one sample t-test to determine whether the viral titer quantification of the untreated condition is significantly different from an undetectable viral load (i.e., viral titer = 0). Note that our data cannot be assumed to be normally distributed. The results indicate there is a significant difference between the untreated and mAb treated mice (e.g., early, late, or prophylactic

treatment). For these analyses, we also calculated the effect size (e.g.,  $r = 0.90$  (large effect size),  $V = 21$ ,  $p$ -value = 0.03).

## Extended Data

Disease parameter	Human COVID-19	Humanized COVID-19	COVID-19 in animal models
Weight loss	>5% of initial body weight	Chronic 10-30% of initial body weight, sustained for weeks	Acute Hamsters <sup>1</sup> : 10% weight loss, recovers in 10 days Mouse adapted SARS-2 virus in mice <sup>2</sup> : 10- 20 % weight loss, recovers in ~10 days
Duration of disease pathology	Weeks to months <sup>3</sup>	>4 weeks	4-10 days
Mortality	0.1% to over 25% case fatality rate based on age, risk factors and country	None detected	Fatal encephalitis in mouse brain upon vector mediated, transient ACE2 expressing model <sup>4</sup>
Lung pathology	Diffuse alveolar damage, perivenular, fibrosis in severe cases <sup>5-8</sup>	Chronic Diffuse alveolar damage, signs of fibrosis with significant cellular infiltrate late in disease	Acute Vector-mediated or transgenic mouse models <sup>9-11</sup> : Mild alveolitis Ferrets <sup>12</sup> : mostly upper respiratory disease with infiltration in alveolar spaces Mouse adapted SARS-2 virus in mice <sup>2</sup> : Acute lung injury, resolves in days
Lymphopenia	T cell lymphopenia <sup>13,14</sup> (CD8+ T cell in particular)	T cell lymphopenia (CD8+ T cell in particular)	None
Macrophage response	Monocytic, inflammatory macrophages as drivers of pathology <sup>15,16</sup>	Monocytic, inflammatory macrophages as drivers of pathology	Monocytes and monocytic macrophages infiltrate the lungs but immunopathology resolves <sup>9</sup>
Cytokines	Increased levels of proinflammatory cytokines/chemokines : IL6, TNF, IL1B, IFN $\gamma$ , MCP-1-CCL2, CXCL10 and others <sup>13,15-17</sup>	Increased levels of proinflammatory cytokines (IL6, TNF, IL1B, IFN $\gamma$ , MCP1 and others)	Increased levels of proinflammatory cytokines (IL6, TNF, IL1B, IFN $\gamma$ , MCP1 and others) particularly in mouse adapted version of SARS-2 <sup>9</sup>
T cell response	Activated T cells with TCR diversity correlating with better prognosis <sup>13,17,18</sup>	Activated T cells	Activated T cells
IFN signature	Sustained for weeks	Sustained for weeks	Sustained for days, responsible for recruitment of Macs <sup>4</sup>
B cell response	Defect in germinal centers <sup>19</sup> ; extrafollicular <sup>20</sup> , highly inflammatory <sup>17,18</sup>	Extrafollicular, highly inflammatory	Germinal center response
Therapeutics (Dexamethasone, Abs)	Dexamethasone <sup>21</sup> : reduced mortality Convalescent and monoclonal Abs <sup>22-24</sup> : limited response, viral clearance	Dexamethasone: timing is crucial to limit immunopathology Convalescent and monoclonal Abs: beneficial as prophylactics and after early administration, late administration provides no benefit, limited response, viral titers reduced or cleared at 4dpi in all applications	Transfer of neutralizing antibodies and mAb stop disease <sup>11</sup> .

### Extended Data Figure 1: Comparison of COVID-19 parameters and response to therapeutics in human patients, humanized mice, and other animal models.

Although substantial anti-viral immunity mediates viral clearance in non-severe COVID-19<sup>2</sup>, robust inflammatory cytokine production, decreased circulating lymphocytes and failure to generate germinal centers characterizes the immunopathology in severe COVID-19<sup>2-4</sup>. Dysregulated myeloid<sup>5-8</sup> and lymphocyte<sup>9-12,56</sup> compartments, including monocytes, macrophages, neutrophils, NK cells and antibody secreting B cells, have been described as players in the observed lung immunopathology of COVID-19. Accurate model systems are essential to rapidly evaluate promising discoveries but most models currently available in mice, ferrets and hamsters do not recapitulate sustained immunopathology described in COVID-19 patients. The following table summarizes various aspects of the human disease and how well these are recapitulated in existing animal models of COVID-19 and in our humanized mouse model of COVID-19.

References:

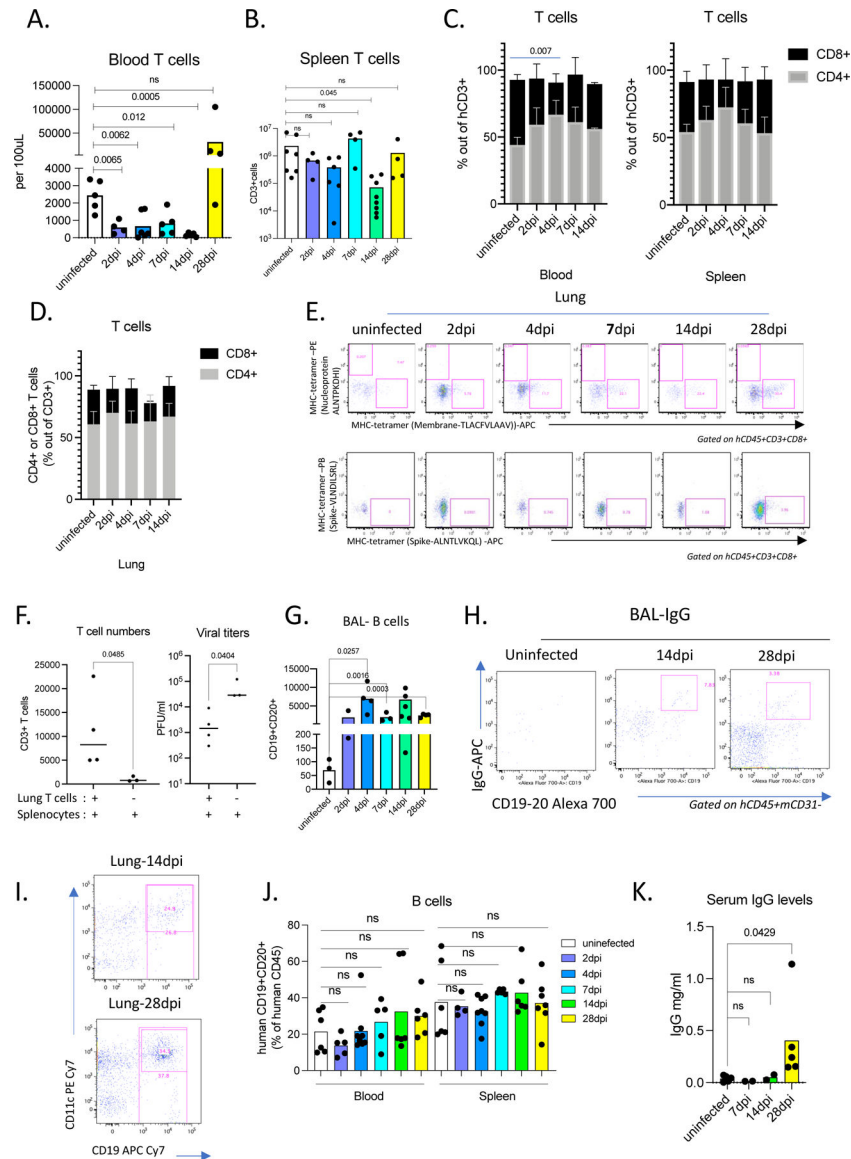
1 Imai, M. *et al.* Syrian hamsters as a small animal model for SARS-CoV-2 infection and countermeasure development. *Proceedings of the National Academy of Sciences* **117**, 16587–16595 (2020).

2 Dinno, K. H. *et al.* A mouse-adapted model of SARS-CoV-2 to test COVID-19 countermeasures. *Nature* **586**, 560–566 (2020).



- 3 Huang, C. *et al.* Clinical features of patients infected with 2019 novel coronavirus in Wuhan, China. *The Lancet* **395**, 497–506, doi:10.1016/S0140–6736(20)30183–5 (2020).
- 4 Song, E. *et al.* Neuroinvasion of SARS-CoV-2 in human and mouse brain. *Journal of Experimental Medicine* **218** (2021).
- 5 Tian, S. *et al.* Pathological study of the 2019 novel coronavirus disease (COVID-19) through postmortem core biopsies. *Modern Pathology*, 1–8 (2020).
- 6 Menter, T. *et al.* Postmortem examination of COVID-19 patients reveals diffuse alveolar damage with severe capillary congestion and variegated findings in lungs and other organs suggesting vascular dysfunction. *Histopathology* **77**, 198–209 (2020).
- 7 Barton, L. M., Duval, E. J., Stroberg, E., Ghosh, S. & Mukhopadhyay, S. Covid-19 autopsies, oklahoma, usa. *American Journal of Clinical Pathology* **153**, 725–733 (2020).
- 8 Xu, Z. *et al.* Pathological findings of COVID-19 associated with acute respiratory distress syndrome. *The Lancet. Respiratory medicine* **8**, 420–422, doi:10.1016/S2213–2600(20)30076-X (2020).
- 9 Israelow, B. *et al.* Mouse model of SARS-CoV-2 reveals inflammatory role of type I interferon signaling. *J Exp Med* **217**, doi:10.1084/jem.20201241 (2020).
- 10 Sun, S.-H. *et al.* A mouse model of SARS-CoV-2 infection and pathogenesis. *Cell Host & Microbe* (2020).
- 11 Hassan, A. O. *et al.* A SARS-CoV-2 infection model in mice demonstrates protection by neutralizing antibodies. *Cell* **182**, 744–753. e744 (2020).
- 12 Ter Meulen, J. *et al.* Human monoclonal antibody as prophylaxis for SARS coronavirus infection in ferrets. *The Lancet* **363**, 2139–2141 (2004).
- 13 Mathew, D. *et al.* Deep immune profiling of COVID-19 patients reveals distinct immunotypes with therapeutic implications. *Science* **369** (2020).
- 14 Tan, L. *et al.* Lymphopenia predicts disease severity of COVID-19: a descriptive and predictive study. *Signal transduction and targeted therapy* **5**, 1–3 (2020).
- 15 Zhang, J.-Y. *et al.* Single-cell landscape of immunological responses in patients with COVID-19. *Nature immunology* **21**, 1107–1118 (2020).
- 16 Liao, M. *et al.* Single-cell landscape of bronchoalveolar immune cells in patients with COVID-19. *Nature medicine*, 1–3 (2020).
- 17 Lucas, C. *et al.* Longitudinal analyses reveal immunological misfiring in severe COVID-19. *Nature* **584**, 463–469 (2020).
- 18 Chen, Z. & Wherry, E. J. T cell responses in patients with COVID-19. *Nature Reviews Immunology*, 1–8 (2020).
- 19 Kaneko, N. *et al.* Loss of Bcl-6-expressing T follicular helper cells and germinal centers in COVID-19. *Cell* **183**, 143–157. e113 (2020).
- 20 Woodruff, M. C. *et al.* Extrafollicular B cell responses correlate with neutralizing antibodies and morbidity in COVID-19. *Nature immunology* **21**, 1506–1516 (2020).
- 21 Group, R. C. Dexamethasone in hospitalized patients with Covid-19—preliminary report. *New England Journal of Medicine* (2020).
- 22 Cruz-Teran, C. *et al.* Challenges and opportunities for antiviral monoclonal antibodies as COVID-19 therapy. *Advanced Drug Delivery Reviews* (2020).
- 23 Casadevall, A. & Pirofski, L.-a. The convalescent sera option for containing COVID-19. *The Journal of clinical investigation* **130** (2020).

24 Chen, P. *et al.* SARS-CoV-2 neutralizing antibody LY-CoV555 in outpatients with Covid-19. *New England Journal of Medicine* (2020).



**Extended data Figure 2 (matched to Figure 3):**

**A.** Numbers of human T cells in the blood pre- and post-infection (2,4,7,14,28dpi). Unpaired, two-tailed t-test. P-values<0.05 are plotted. Uninfected n=5, 2dpi n=4, 4dpi n=6, 7dpi n=5, 14dpi n=5, 28dpi=4, biologically independent mice examined over at least 3 independent experiments. Individual values for each mouse and means are plotted.

**B.** Numbers of human T cells in the spleens of uninfected or infected mice (2,4,7,14,28dpi). Unpaired, two-tailed t-test. P-values<0.05 are plotted. Unpaired, two-tailed t-test. Only p-values<0.05 are plotted. Uninfected n=7, 2dpi n=4, 4dpi n=6, 7dpi n=4, 14dpi n=8, 28dpi=4, biologically independent mice examined over at least 3 independent experiments. Individual values for each mouse and means are plotted.

**C.** Frequencies of human CD4<sup>+</sup> or CD8<sup>+</sup> T cells within hCD3<sup>+</sup> population in the blood and spleens of uninfected or infected mice at 2,4,7,14,28 dpi. Blood: N=4 biologically independent mice examined over at least 2 independent experiments. Means with SD are plotted. Spleen: Uninfected n=5, 2dpi n=4, 4dpi n=6, 7dpi n=4, 14dpi n=4 biologically independent mice examined over at least 3 independent experiments. Individual values for each mouse and means are plotted.

**D.** Frequencies of human CD4<sup>+</sup> or CD8<sup>+</sup> T cells within hCD3<sup>+</sup> population in the lungs of uninfected or infected mice at 2,4,7,14,28 dpi. Uninfected n=4, 2dpi n=4, 4dpi n=6, 7dpi n=4, 14dpi n=4 biologically independent mice examined over 3 independent experiments. Individual values for each mouse and means are plotted.

**E.** Representative flow cytometry plots of CD8<sup>+</sup> T cells stained with viral antigen bearing HLA-A2 tetramers. HLA-A2 tetramers bound to peptides of Nucleoprotein(N), Membrane protein(M) and Spike protein were used to characterize T cells from uninfected and infected (2,4,7,14,28dpi) mice. Representative of uninfected n=3, 2dpi n=2, 4dpi n=3, 7dpi n=3, 14dpi n=3, 28dpi n=3 biologically independent mice examined over 2 independent experiments.

**F.** T cell numbers and viral titers following prophylactic T cell transfer in infected mice at 4dpi. Splenocytes and sorted T cells from lungs of 14dpi mice where the contribution of the antigen specific B cell response was minimal were transferred to unengrafted MISTRG-hACE2 (no human immune cells prior to transfer). Control MISTRG-hACE2 mice received splenocytes but not sorted lung T cells (n=3 biologically independent mice examined over 2 independent experiments). These mice were subsequently infected and analyzed at 4dpi for viral titers and human immune cells in lungs. In mice that received sorted lung T cells, human immune compartment in lungs comprised of T cells and few CD16<sup>+</sup> monocytes and macrophages but no B cells (n=4 biologically independent mice examined over 2 independent experiments).

**G.** Numbers of human B cells in the BAL of uninfected or infected mice at 2,4,7,14,28 dpi. N=3–6. Unpaired, two-tailed t-test. P-values<0.05 are plotted. Uninfected n=3, 2dpi n=3, 4dpi n=4, 7dpi n=3, 14dpi n=7, 28dpi n=4 biologically independent mice examined over at least 3 independent experiments. Individual values for each mouse and means are plotted.

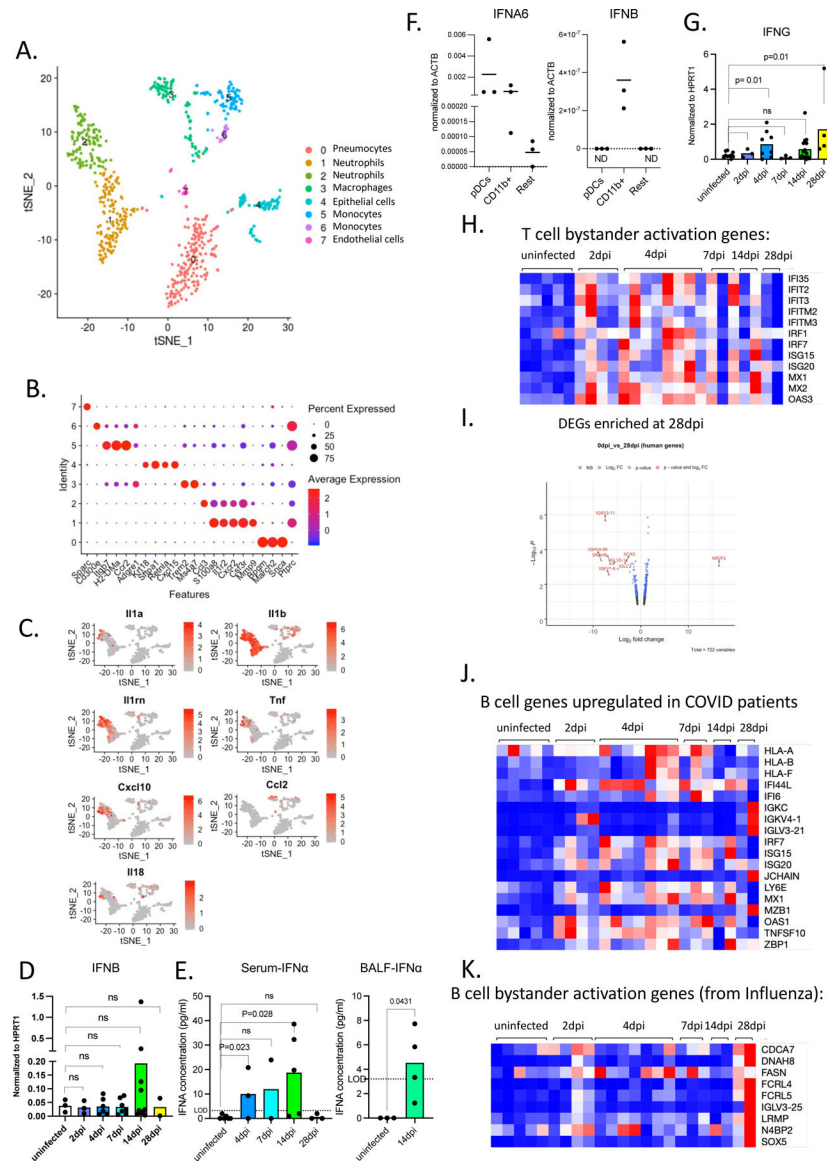
**H.** Representative flow cytometry plots of IgG<sup>+</sup> B cells in the BAL of uninfected and infected mice 14 and 28dpi. Representative of n=4 biologically independent mice examined over 3 independent experiments.

**I.** CD11C and CD19 expression on human immune cells from infected lungs at 14 and 28 dpi. N=4–5. Representative of n=5 (14dpi) and n=4 (28dpi) biologically independent mice examined over at least 3 independent experiments.

**J.** Frequencies of human B cells marked by CD19 and CD20 expression within hCD45<sup>+</sup> population in spleen and blood of uninfected or infected mice at 2,4,7,14,28 dpi. Blood: Uninfected n=6, 2dpi n=5, 4dpi n=8, 7dpi n=5, 14dpi n=6, 28dpi n=6 biologically independent mice examined over at least 3 independent experiments. Spleen: Uninfected n=6, 2dpi n=4, 4dpi n=8, 7dpi n=5, 14dpi n=6, 28dpi n=7 biologically independent mice examined over at least 3 independent experiments. Individual values for each mouse and means are plotted.

**K.** IgG levels measured by ELISA in serum of uninfected or infected mice at 7,14, 28 dpi. Uninfected n=5, 7dpi n=2, 14dpi n=2, 28dpi n=5 biologically independent mice examined

over 2 independent experiments. Individual values for each mouse and means are plotted. Unpaired, two tailed t-test.



#### Extended Data Figure 3 (matched to Figure 4):

A. t-distributed stochastic neighbor embedding (t-SNE) plot with clustering results of single cell RNA sequencing of mouse cells from lungs at 4dpi. Single cell suspensions from whole infected lung at 4dpi were processed and sequenced. There were 731 cells identified as mouse cells.

B. Dot plot of cluster identifying genes for mouse cell clusters described in S4A.

C. Cluster distribution and expression profile of mouse inflammatory cytokines for clusters described in 4B.

D. Normalized expression of human IFNB measured by qPCR in homogenized lung tissue of uninfected and infected (2,4,7,14,28dpi) mice. Expression was normalized to human HPRT1. Unpaired t-test, one-tailed since the distribution is expected to be one-sided.

Uninfected n=3, 2dpi n=3, 4dpi n=6, 7dpi n=7, 14dpi n=10, 28dpi n=2 biologically independent mice examined over at least 3 independent experiments. Individual values for each mouse and means are presented. P-values<0.05 are plotted.

E. IFNA levels measured by ELISA in serum and BAL of uninfected or infected mice.

Serum: Uninfected n=6, 4dpi n=3, 7dpi n=2, 14dpi n=5, 28dpi n=3; BAL: Uninfected n=3, 14dpi n=4 biologically independent mice examined over at least 2 independent experiments for all time points. Individual values (average of duplicates) for each mouse and means are plotted.

F. Type I interferon levels (IFNA6 and IFNB) per cell measured by qPCR in sorted human immune cells (human CD45+): plasmacytoid dendritic cells (PDCs; CD123<sup>hi</sup> CD11B-), macrophages and monocytes (CD11B+) and rest of human immune cells (CD123-CD11B-CD45+). Expression was normalized to human ACTB. Individual values and means are plotted. n=3 biologically independent mice examined over 2 independent experiments. Individual values with means are plotted.

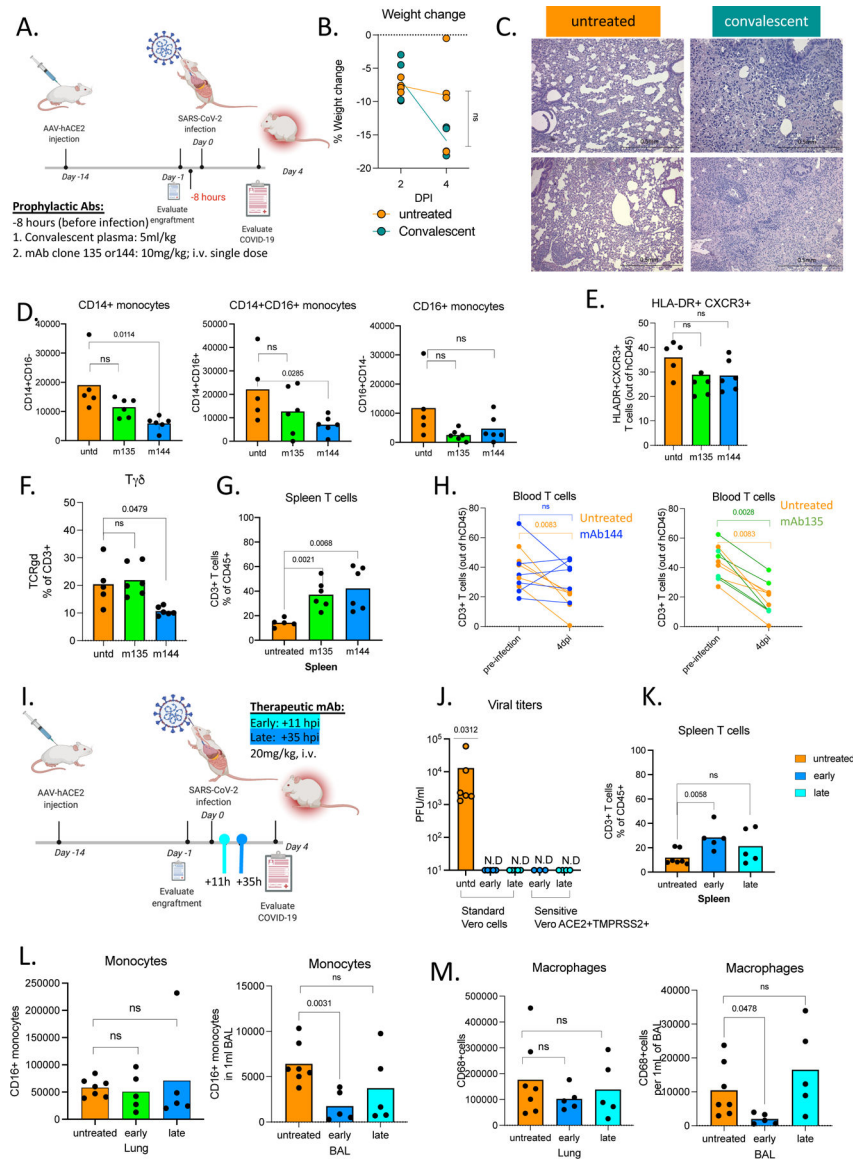
G. Normalized expression of human IFNG measured by qPCR in homogenized lung tissue of uninfected and infected (2,4,7,14,28dpi) mice. Expression was normalized to human HPRT1. Unpaired t-test, one tailed since distribution is expected to be one-sided. Uninfected n=10, 2dpi n=3, 4dpi n=8, 7dpi n=3, 14dpi n=15, 28dpi n=5 biologically independent mice examined over at least 3 independent experiments for all time points.

H. Heatmap of normalized counts for bystander activated memory T cell signature genes<sup>67</sup>(based on Low et al., JEM 2020) in lungs of MISTRG6-hACE2 mice infected with SARS-CoV-2. Row min and max of transformed values, calculated by subtracting row mean and dividing by STD for each gene across all samples, are visualized. Uninfected n=5, 2dpi n=4, 4dpi n=7, 7dpi n=3, 14dpi n=2, 28dpi n=2 biologically independent mice examined over at least 2 independent experiments for all time points.

I. Volcano plot showing foldchange and adjusted p-values (by Wald test using DESeq2) of differentially regulated genes at 28dpi compared to uninfected lungs. Genes with FC(Log2)>1 and p value<0.05 are highlighted in red. Replicates of at least 2 mice. Uninfected n=5, 28dpi n=2 biologically independent mice examined over 2 independent experiments.

J. Heatmap of normalized counts for genes that are induced in B cells of patients with moderate or severe COVID-19 in comparison with healthy controls. Normalized counts in lungs of uninfected or infected MISTRG6-hACE2 were plotted over the course of infection. Row min and max of transformed values, calculated by subtracting row mean and dividing by STD for each gene across all samples, are visualized. Uninfected n=5, 2dpi n=4, 4dpi n=7, 7dpi n=3, 14dpi n=2, 28dpi n=2 biologically independent mice examined over at least 2 independent experiments for all time points.

K. Heatmap of normalized counts for bystander activated memory B cell signature genes<sup>68</sup>(based on Horns et al., 2020) in lungs of MISTRG6-hACE2 mice infected with SARS-CoV-2. Row min and max of transformed values, calculated by subtracting row mean and dividing by STD for each gene across all samples, are visualized. Uninfected n=5, 2dpi n=4, 4dpi n=7, 7dpi n=3, 14dpi n=2, 28dpi n=2 biologically independent mice examined over at least 2 independent experiments for all time points.



### Extended Date Figure 4 (matched to Figure 5):

A. Schematic of experimental design of prophylactic antibody treatment MISTRG6-hACE2 mice received prophylactic treatment of convalescent plasma (5ml/kg) or monoclonal antibodies at 10mg/kg (clone 135 -m135 or clone 144-m144) 8 hours prior to infection or left untreated (unt). Mice were euthanized 4dpi. Convalescent plasma samples from the top 30 neutralizers in a cohort of 148 individuals were pooled to create a mixture with an NT50 titer of 1597 against HIV-1 pseudotyped with SARS-CoV-2 S protein<sup>72</sup>. Sequencing the antibody genes from infected humans has revealed the expansion of closely related Receptor Binding Domain of the Spike protein (RBD)-specific B cell antibody clones in different SARS-CoV-2 infected individuals. Although most convalescent plasma samples obtained from patients who recovered from COVID-19 did not contain high levels of neutralizing activity, RBD-specific antibodies with potent antiviral activity were found in all individuals tested<sup>72</sup>. Monoclonal recombinant antibodies (mAbs) used in this study were cloned from

these convalescent patients and had high neutralizing activity against SARS-CoV-2 *in vitro* and *in vivo* in mouse adapted SARS-CoV-2 infection<sup>72,76</sup>.

B. Weight change in convalescent plasma treated mice at 2 and 4dpi plotted as percent change compared with original weight measured just before inoculation with SARS-CoV-2. Unpaired t-test, two-tailed comparing 4dpi values. N=4 biologically independent mice examined over 2 independent experiments for all time points. Individual values per each mouse plotted.

C. Representative images (10x magnification) of H&E staining of lungs (4dpi) from mice treated prophylactically with convalescent plasma or left untreated. The histopathological findings mark transition into the organizing phase, highlighted by infiltration of the inter- and intra-alveolar space by lymphocytes macrophages, and fibroblasts. Representative of N=4 biologically independent mice examined over 2 independent experiments for all time points. Individual values for each mouse are plotted.

D. Frequencies of human monocytes (CD14+ classical; CD14+CD16+ intermediate, CD16+ non classical) within human CD45+ cells in the lungs of MISTRG6-hACE2 mice which received a prophylactic treatment of monoclonal antibody clone 135 (m135) or clone 144(m144) 8 hours prior to infection or left untreated (untreated). Unpaired, two-tailed t-test. P-values<0.05 are plotted. Untreated N=5, treated n=6 N=4 biologically independent mice examined over 2 independent experiments for all time points. Individual values for each mouse and means are plotted.

E. Frequencies of HLA-DR+CXCR3+ T cells within human CD3+CD45+ cells in lungs of MISTRG6-hACE2 mice which received a prophylactic treatment of monoclonal antibody clone 135 (m135) or clone 144(m144) 8 hours prior to infection or left untreated (untreated). Unpaired, two-tailed t-test. N=5–6. P-values<0.05 are plotted. Untreated N=5, treated n=6 N=4 biologically independent mice examined over 2 independent experiments for all time points. Individual values for each mouse and means are plotted.

F. Frequencies of T $\gamma\delta$  cells within human CD3+CD45+ cells in lungs of MISTRG6-hACE2 mice which received prophylactic treatment of monoclonal antibody clone 135 (m135) or clone 144(m144) 8 hours prior to infection or left untreated (untreated). Unpaired, two-tailed t-test. N=5–6. P-values<0.05 are plotted. Untreated N=5, treated n=6 N=4 biologically independent mice examined over 2 independent experiments for all time points. Individual values for each mouse and means are plotted.

G. Frequencies of human T cells within human CD45+ cells in spleens of MISTRG6-hACE2 mice received a prophylactic treatment of monoclonal antibody clone 135 (m135) or clone 144(m144) 8 hours prior to infection or left untreated (untreated). Unpaired, two-tailed t-test. N=5–6. P-values<0.05 are plotted. Untreated N=5, treated n=6 N=4 biologically independent mice examined over 2 independent experiments for all time points. Individual values for each mouse and means are plotted.

H. Frequencies of human CD3+ T cells within human CD45+ population in the blood pre- and post-infection (2,4,7,14,28dpi). Lines connect pre- and post-infection values for the same mouse. MISTRG6-hACE2 mice received a prophylactic treatment of monoclonal antibody clone 135 (m135) or clone 144(m144) 8 hours prior to infection or left untreated (untreated). Paired, two-tailed t-test. P-values<0.05 are plotted. Untreated N=5, treated n=6 N=4 biologically independent mice examined over 2 independent experiments for all time points. Individual values for each mouse are plotted.

I. Schematic of experimental design of post-infection mAb treatment. MISTRG6-hACE2 mice received a mixed cocktail of monoclonal antibodies clone 135 (m135) and clone 144(m144) at 20mg/kg or left untreated (untd). Early treatment groups were treated 11 hours post-infection and late treatment 35 hours post-infection. Monoclonal recombinant antibodies (mAbs) used in this study were cloned from the convalescent patients (whose plasma was used prophylactically before) and had high neutralizing activity against SARS-CoV-2 *in vitro* and *in vivo* in mouse adapted SARS-CoV-2 infection <sup>72,76</sup>.

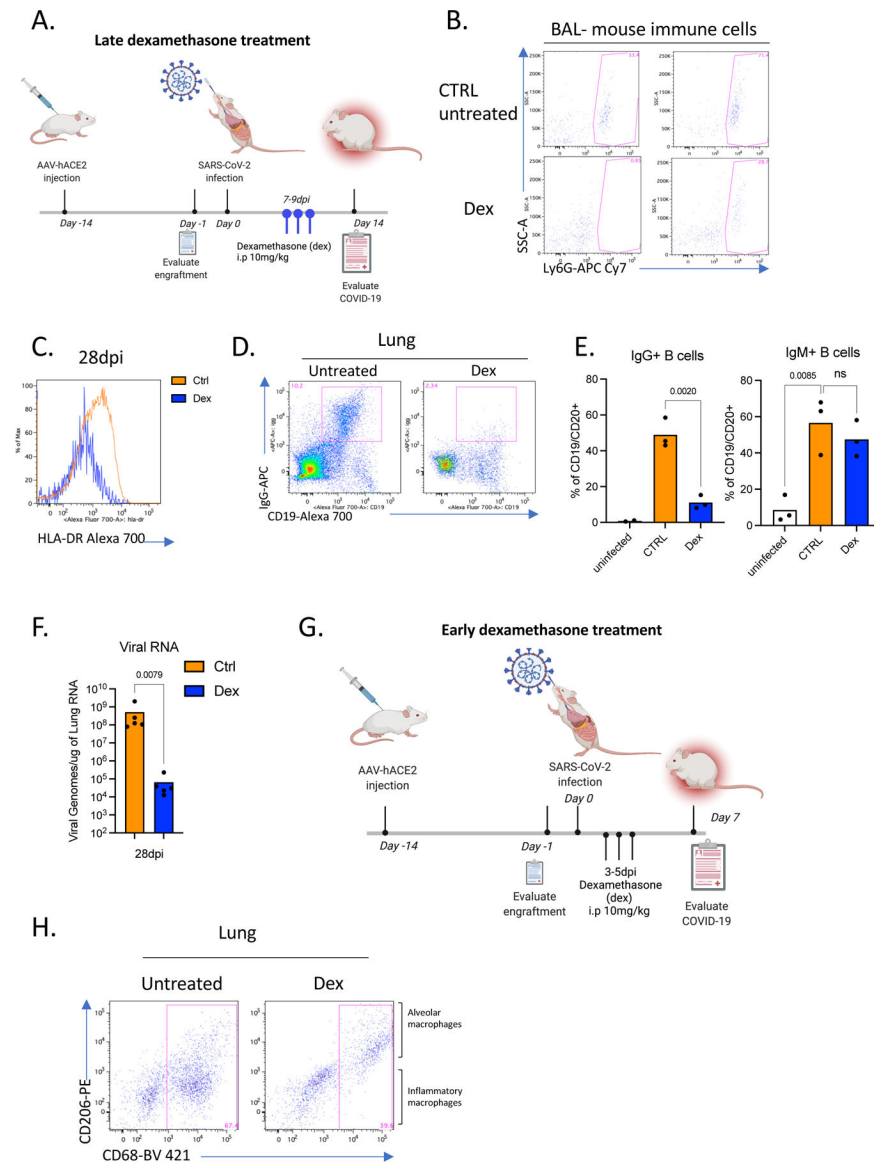
J. Viral titers measured by PFU in homogenized lung tissue following early or late therapeutic mAb at 4dpi using Vero E6 (standard assay) Vero-ACE2+TMPRSS2+ (sensitive assay) cells. N=4 biologically independent mice examined over 2 independent experiments measurement with Vero-ACE2+TMPRSS2+ (sensitive assay) cells. Individual values for each mouse are plotted.

K. Frequencies of human T cells within human CD45+ cells in spleens of MISTRG6-hACE2 mice that received early, late or no treatment of monoclonal antibody mix. Unpaired, two-tailed t-test. Untreated n=7, treated n=5 biologically independent mice examined over 3 independent experiments for all time points. Pooled, infection-matched mice are presented. P-values<0.05 are plotted. Individual values representing each mouse are plotted. Individual values for each mouse are plotted.

L. Number of CD16+ human monocytes in lungs of treated and untreated mice at 4dpi. Mice were either MISTRG6-hACE2 mice that received a mixed cocktail of monoclonal antibodies clone 135 (m135) and clone 144(m144) or left untreated (untd). Early treatment group was treated 11 hours post-infection (hpi) and late treatment 35 hpi. Unpaired, two-tailed t-test. Untreated n=7, treated n=5 biologically independent mice examined over 3 independent experiments for all time points. Pooled, infection-matched mice are presented. P-values<0.05 are plotted. Individual values representing each mouse are plotted.

M. Number of human macrophages in lungs of treated and untreated mice at 4dpi. MISTRG6-hACE2 mice that received a mixed cocktail of monoclonal antibodies clone 135 (m135) and clone 144(m144) or left untreated (untd). Early treatment group was treated 11 hours post-infection and late treatment 35 hours post-infection. Unpaired, two-tailed t-test. Untreated n=7, treated n=5 biologically independent mice examined over 3 independent experiments for all time points. Pooled, infection-matched mice are presented. P-values<0.05 are plotted. Individual values representing each mouse are plotted.



**Extended data Figure 5 (matched to Figure 6):**

A. Schematic of experimental design of dexamethasone treatment: SARS-CoV-2 infected MISTRG6-hACE2 mice were either treated with dexamethasone on days 7,8,9 post-infection or left untreated. Mice were analyzed either at 14dpi or 28dpi. Mice were treated intraperitoneally (i.p.) with dexamethasone at 10mg/kg dose.

B. Representative flow cytometry plots of Ly6G expressing SSChi cells (mouse neutrophils) within the mouse immune cell population (mouse CD45+) in the BAL of dexamethasone treated or control untreated mice. Representative of 4 biologically independent mice examined over at least 2 independent experiments.

C. HLA-DR expression on lung T cells 28dpi in dexamethasone treated or control mice. Representative of 3 biologically independent mice examined over at least 2 independent experiments.

D. Representative flow cytometry plots of Surface IgG and CD19 expression on human immune cells gated on hCD45+ cells in lungs of untreated or dexamethasone treated mice at 28dpi. N=3 of biologically independent mice examined over at least 2 independent experiments.

E. Frequencies of IgM+ and IgG+ B cells in lungs of untreated or dexamethasone treated mice at 28dpi. Mice were treated with dexamethasone on days 7,8,9 post-infection. N=3 biologically independent mice examined over at least 2 independent experiments. Unpaired t-test, two-tailed.

F. Viral RNA in the lung homogenates of dexamethasone treated or control untreated mice at 28dpi. Mann-Whitney, two-tailed test. N=5 biologically independent mice examined over 3 independent experiments.

G. Schematic of experimental design of SARS-CoV-2 infected MISTRG6-hACE2 mice either treated with dexamethasone on days 3,4,5 dpi or left untreated.

H. CD206 and CD68 expression in lung human immune cells in mice treated with dexamethasone or left untreated at 7dpi. CD206hi+ CD68+ cells are alveolar macrophages. Treated N=4, untreated N=6 biologically independent mice examined over 2 independent experiments. Alveolar macrophages are marked by high CD206 expression. Inflammatory macrophages are enriched in the CD206 negative population which also express CD86 (not shown).

## Supplementary Material

Refer to Web version on PubMed Central for supplementary material.

## Acknowledgements:

The generation of the original MISTRG6 model was supported by the Bill and Melinda Gates Foundation. We thank G. Yancopoulos, D. Valenzuela, A. Murphy, and W. Auerbach at Regeneron Pharmaceuticals who generated, in collaboration with our groups, the individual knock-in alleles combined in MISTRG. We thank H. Steach, M. Chiorazzi, I. Odell, E. Eynon, and W. Philbrick and all the other members of the Flavell lab for discussions and comments; J. Alderman, C. Lieber, B. Cadugan and E. Hughes-Picard for administrative assistance; P. Ranney, C. Hughes for mouse colony management; D. Urbanos for human CD34+ cell isolation; L. Devine for help with cell sorting. E. Sefik is a HHMI Fellow of the Damon Runyon Cancer Research Foundation (DRG-2316-18). This work was funded by the Howard Hughes Medical Institute (RAF, MN, and AI). This study was also supported in part by awards from National Institute of Health grants, R01AI157488 (AI), F30CA239444 (ES), 2T32AI007517, K08AI163493 (BI), AI061093(EM), AI118855(EM), CA016359 (EM), K08 AI128043 (CBW), U01 CA260507 (SH), Burroughs Wellcome Fund (CBW), Patterson Foundation (CBW), Fast Grant from Emergent Ventures at the Mercatus Center (AI, ES, CBW), Mathers Foundation (AI, CBW, EM), and the Ludwig Family Foundation (AI, CBW).

## Data Availability:

All data that support the findings of this study are available within the paper and its Supplementary Information files. The data supporting this publication is available at [Figshare.com](https://figshare.com/projects/A_humanized_mouse_model_of_COVID-19/125659) under project “A Humanized Mouse Model of COVID-19” ([https://figshare.com/projects/A\\_humanized\\_mouse\\_model\\_of\\_COVID-19/125659](https://figshare.com/projects/A_humanized_mouse_model_of_COVID-19/125659)).

All 10x Genomics single cell RNA sequencing and bulk RNA sequencing data that support the findings of this study was deposited in the Gene Expression Omnibus (GEO) repository with accession codes GSE186794.

## References:

1. Letko M, Marzi A & Munster V Functional assessment of cell entry and receptor usage for SARS-CoV-2 and other lineage B betacoronaviruses. *Nature microbiology* 5, 562–569 (2020).
2. Huang C et al. Clinical features of patients infected with 2019 novel coronavirus in Wuhan, China. *The Lancet* 395, 497–506, doi:10.1016/S0140-6736(20)30183-5 (2020).
3. Mehta P et al. COVID-19: consider cytokine storm syndromes and immunosuppression. *The Lancet* (2020).
4. Xu Z et al. Pathological findings of COVID-19 associated with acute respiratory distress syndrome. *The Lancet. Respiratory medicine* 8, 420–422, doi:10.1016/S2213-2600(20)30076-X (2020). [PubMed: 32085846]
5. Schulte-Schrepping J et al. Severe COVID-19 is marked by a dysregulated myeloid cell compartment. *Cell* 182, 1419–1440. e1423 (2020). [PubMed: 32810438]
6. Del Valle DM et al. An inflammatory cytokine signature predicts COVID-19 severity and survival. *Nat Med* 26, 1636–1643, doi:10.1038/s41591-020-1051-9 (2020). [PubMed: 32839624]
7. Liao M et al. Single-cell landscape of bronchoalveolar immune cells in patients with COVID-19. *Nature medicine*, 1–3 (2020).
8. Zhang JY et al. Single-cell landscape of immunological responses in patients with COVID-19. *Nat Immunol* 21, 1107–1118, doi:10.1038/s41590-020-0762-x (2020). [PubMed: 32788748]
9. Chua RL et al. COVID-19 severity correlates with airway epithelium-immune cell interactions identified by single-cell analysis. *Nat Biotechnol* 38, 970–979, doi:10.1038/s41587-020-0602-4 (2020). [PubMed: 32591762]
10. Lucas C et al. Longitudinal analyses reveal immunological misfiring in severe COVID-19. *Nature* 584, 463–469 (2020). [PubMed: 32717743]
11. Chen Z & Wherry EJ T cell responses in patients with COVID-19. *Nature Reviews Immunology*, 1–8 (2020).
12. Mathew D et al. Deep immune profiling of COVID-19 patients reveals distinct immunotypes with therapeutic implications. *Science* 369 (2020).
13. Delorey TM et al. COVID-19 tissue atlases reveal SARS-CoV-2 pathology and cellular targets. *Nature* 595, 107–113, doi:10.1038/s41586-021-03570-8 (2021). [PubMed: 33915569]
14. McCray PB et al. Lethal infection of K18-hACE2 mice infected with severe acute respiratory syndrome coronavirus. *Journal of virology* 81, 813–821 (2007). [PubMed: 17079315]
15. Goldman-Israelow B et al. Mouse model of SARS-CoV-2 reveals inflammatory role of type I interferon signaling. *bioRxiv* (2020).
16. Bao L et al. The pathogenicity of SARS-CoV-2 in hACE2 transgenic mice. *Nature* 583, 830–833, doi:10.1038/s41586-020-2312-y (2020). [PubMed: 32380511]
17. Hassan AO et al. A SARS-CoV-2 infection model in mice demonstrates protection by neutralizing antibodies. *Cell* 182, 744–753. e744 (2020). [PubMed: 32553273]
18. Israelow B et al. Mouse model of SARS-CoV-2 reveals inflammatory role of type I interferon signaling. *J Exp Med* 217, doi:10.1084/jem.20201241 (2020).
19. Sun S-H et al. A mouse model of SARS-CoV-2 infection and pathogenesis. *Cell Host & Microbe* (2020).
20. Imai M et al. Syrian hamsters as a small animal model for SARS-CoV-2 infection and countermeasure development. *Proceedings of the National Academy of Sciences* 117, 16587–16595 (2020).
21. Rockx B et al. Comparative pathogenesis of COVID-19, MERS, and SARS in a nonhuman primate model. *Science* 368, 1012–1015 (2020). [PubMed: 32303590]
22. Xu H et al. High expression of ACE2 receptor of 2019-nCoV on the epithelial cells of oral mucosa. *International Journal of Oral Science* 12, 8–8, doi:10.1038/s41368-020-0074-x (2020). [PubMed: 32094336]
23. Yan R et al. Structural basis for the recognition of SARS-CoV-2 by full-length human ACE2. *Science* 367, 1444–1448, doi:10.1126/science.abb2762 (2020). [PubMed: 32132184]

24. Hoffmann M et al. SARS-CoV-2 Cell Entry Depends on ACE2 and TMPRSS2 and Is Blocked by a Clinically Proven Protease Inhibitor. *Cell* 181, 271–280 e278, doi:10.1016/j.cell.2020.02.052 (2020). [PubMed: 32142651]
25. Yang XH et al. Mice transgenic for human angiotensin-converting enzyme 2 provide a model for SARS coronavirus infection. *Comp Med* 57, 450–459 (2007). [PubMed: 17974127]
26. Li W et al. Efficient replication of severe acute respiratory syndrome coronavirus in mouse cells is limited by murine angiotensin-converting enzyme 2. *J Virol* 78, 11429–11433, doi:10.1128/JVI.78.20.11429-11433.2004 (2004). [PubMed: 15452268]
27. Theocharides AP, Rongvaux A, Fritsch K, Flavell RA & Manz MG Humanized hemato-lymphoid system mice. *Haematologica* 101, 5–19, doi:10.3324/haematol.2014.115212 (2016). [PubMed: 26721800]
28. Rongvaux A et al. Human hemato-lymphoid system mice: current use and future potential for medicine. *Annu Rev Immunol* 31, 635–674, doi:10.1146/annurev-immunol-032712-095921 (2013). [PubMed: 23330956]
29. Rongvaux A et al. Development and function of human innate immune cells in a humanized mouse model. *Nature Biotechnology* 32, 364–372, doi:10.1038/nbt.2858 (2014).
30. Rathinam C et al. Efficient differentiation and function of human macrophages in humanized CSF-1 mice. doi:10.1182/blood-2010-12-326926 (2011).
31. Willinger T et al. Human IL-3/GM-CSF knock-in mice support human alveolar macrophage development and human immune responses in the lung. *Proceedings of the National Academy of Sciences of the United States of America* 108, 2390–2395, doi:10.1073/pnas.1019682108 (2011). [PubMed: 21262803]
32. Strowig T et al. Transgenic expression of human signal regulatory protein alpha in Rag2-/-gamma(c)-/- mice improves engraftment of human hematopoietic cells in humanized mice. *Proceedings of the National Academy of Sciences of the United States of America* 108, 13218–13223, doi:10.1073/pnas.1109769108 (2011). [PubMed: 21788509]
33. Rongvaux A et al. Human thrombopoietin knockin mice efficiently support human hematopoiesis in vivo. *Proceedings of the National Academy of Sciences of the United States of America* 108, 2378–2383, doi:10.1073/pnas.1019524108 (2011). [PubMed: 21262827]
34. Rongvaux A et al. Development and function of human innate immune cells in a humanized mouse model. *Nat Biotechnol* 32, 364–372, doi:10.1038/nbt.2858 (2014). [PubMed: 24633240]
35. Yu H et al. A novel humanized mouse model with significant improvement of class-switched, antigen-specific antibody production. *Blood* 129, 959–969, doi:10.1182/blood-2016-04-709584 (2017). [PubMed: 28077418]
36. Das R et al. Microenvironment-dependent growth of preneoplastic and malignant plasma cells in humanized mice. *Nat Med* 22, 1351–1357, doi:10.1038/nm.4202 (2016). [PubMed: 27723723]
37. Sippel TR, Radtke S, Olsen TM, Kiem H-P & Rongvaux A Human hematopoietic stem cell maintenance and myeloid cell development in next-generation humanized mouse models. *Blood advances* 3, 268 (2019). [PubMed: 30696625]
38. Roberts A et al. A mouse-adapted SARS-coronavirus causes disease and mortality in BALB/c mice. *PLoS Pathog* 3, e5, doi:10.1371/journal.ppat.0030005 (2007). [PubMed: 17222058]
39. Polak SB, Van Gool IC, Cohen D, von der Thusen JH & van Paassen J A systematic review of pathological findings in COVID-19: a pathophysiological timeline and possible mechanisms of disease progression. *Mod Pathol* 33, 2128–2138, doi:10.1038/s41379-020-0603-3 (2020). [PubMed: 32572155]
40. Tian S et al. Pathological study of the 2019 novel coronavirus disease (COVID-19) through postmortem core biopsies. *Modern Pathology*, 1–8 (2020).
41. Menter T et al. Postmortem examination of COVID-19 patients reveals diffuse alveolar damage with severe capillary congestion and variegated findings in lungs and other organs suggesting vascular dysfunction. *Histopathology* 77, 198–209 (2020). [PubMed: 32364264]
42. Barton LM, Duval EJ, Stroberg E, Ghosh S & Mukhopadhyay S Covid-19 autopsies, oklahoma, usa. *American Journal of Clinical Pathology* 153, 725–733 (2020). [PubMed: 32275742]
43. Nathan C Neutrophils and COVID-19: Nots, NETs, and knots. *J Exp Med* 217, doi:10.1084/jem.20201439 (2020).

44. Shafran N et al. Secondary bacterial infection in COVID-19 patients is a stronger predictor for death compared to influenza patients. *Sci Rep* 11, 12703, doi:10.1038/s41598-021-92220-0 (2021). [PubMed: 34135459]
45. Russell CD et al. Co-infections, secondary infections, and antimicrobial use in patients hospitalised with COVID-19 during the first pandemic wave from the ISARIC WHO CCP-UK study: a multicentre, prospective cohort study. *Lancet Microbe*, doi:10.1016/S2666-5247(21)00090-2 (2021).
46. Baharom F et al. Dendritic cells and monocytes with distinct inflammatory responses reside in lung mucosa of healthy humans. *The Journal of Immunology* 196, 4498–4509 (2016). [PubMed: 27183618]
47. Villani AC et al. Single-cell RNA-seq reveals new types of human blood dendritic cells, monocytes, and progenitors. *Science* 356, doi:10.1126/science.aah4573 (2017).
48. Zhou Z et al. Heightened Innate Immune Responses in the Respiratory Tract of COVID-19 Patients. *27*, 883–890 e882, doi:10.1016/j.chom.2020.04.017 (2020).
49. Nienhold R et al. Two distinct immunopathological profiles in autopsy lungs of COVID-19. *Nature communications* 11, 1–13 (2020).
50. Tan L et al. Lymphopenia predicts disease severity of COVID-19: a descriptive and predictive study. *Signal transduction and targeted therapy* 5, 1–3 (2020). [PubMed: 32296011]
51. Wang S et al. IL-21 drives expansion and plasma cell differentiation of autoreactive CD11c hi T-bet+ B cells in SLE. *Nature communications* 9, 1–14 (2018).
52. Jenks SA et al. Distinct effector B cells induced by unregulated toll-like receptor 7 contribute to pathogenic responses in systemic lupus erythematosus. *Immunity* 49, 725–739. e726 (2018). [PubMed: 30314758]
53. Woodruff MC et al. Extrafollicular B cell responses correlate with neutralizing antibodies and morbidity in COVID-19. *Nature immunology* 21, 1506–1516 (2020). [PubMed: 33028979]
54. Schultheiß C et al. Next-generation sequencing of T and B cell receptor repertoires from COVID-19 patients showed signatures associated with severity of disease. *Immunity* 53, 442–455. e444 (2020). [PubMed: 32668194]
55. Stephens DS & McElrath MJ COVID-19 and the Path to Immunity. *Jama* 324, 1279–1281 (2020). [PubMed: 32915201]
56. Grant RA et al. Circuits between infected macrophages and T cells in SARS-CoV-2 pneumonia. *Nature*, 1–10.
57. Dolan ME et al. Investigation of COVID-19 comorbidities reveals genes and pathways coincident with the SARS-CoV-2 viral disease. *Scientific reports* 10, 1–11 (2020). [PubMed: 31913322]
58. Rodero MP et al. Detection of interferon alpha protein reveals differential levels and cellular sources in disease. *J Exp Med* 214, 1547–1555, doi:10.1084/jem.20161451 (2017). [PubMed: 28420733]
59. Peiffer-Smadja N & Yazdanpanah Y Nebulised interferon beta-1a for patients with COVID-19. *The Lancet Respiratory Medicine* (2020).
60. Davoudi-Monfared E et al. A randomized clinical trial of the efficacy and safety of interferon  $\beta$ -1a in treatment of severe COVID-19. *Antimicrobial agents and chemotherapy* 64 (2020).
61. Acharya D, Liu G & Gack MU Dysregulation of type I interferon responses in COVID-19. *Nature Reviews Immunology* 20, 397–398 (2020).
62. Blanco-Melo D et al. Imbalanced host response to SARS-CoV-2 drives development of COVID-19. *Cell* (2020).
63. McNab F, Mayer-Barber K, Sher A, Wack A & O'Garra A Type I interferons in infectious disease. *Nat Rev Immunol* 15, 87–103, doi:10.1038/nri3787 (2015). [PubMed: 25614319]
64. Major J et al. Type I and III interferons disrupt lung epithelial repair during recovery from viral infection. *Science* 369, 712–717, doi:10.1126/science.abc2061 (2020). [PubMed: 32527928]
65. Huang W et al. The Inflammatory Factors Associated with Disease Severity to Predict COVID-19 Progression. *J Immunol* 206, 1597–1608, doi:10.4049/jimmunol.2001327 (2021). [PubMed: 33579725]

66. Leisman DE et al. Cytokine elevation in severe and critical COVID-19: a rapid systematic review, meta-analysis, and comparison with other inflammatory syndromes. *The Lancet Respiratory Medicine* (2020).
67. Low JS et al. Tissue-resident memory T cell reactivation by diverse antigen-presenting cells imparts distinct functional responses. *Journal of Experimental Medicine* 217 (2020).
68. Horns F, Dekker CL & Quake SR Memory B cell activation, broad anti-influenza antibodies, and bystander activation revealed by single-cell transcriptomics. *Cell Reports* 30, 905–913. e906 (2020). [PubMed: 31968262]
69. Zhang J-Y et al. Single-cell landscape of immunological responses in patients with COVID-19. *Nature immunology* 21, 1107–1118 (2020). [PubMed: 32788748]
70. Kaneko N et al. Loss of Bcl-6-expressing T follicular helper cells and germinal centers in COVID-19. *Cell* 183, 143–157. e113 (2020). [PubMed: 32877699]
71. Hutcheson J et al. Combined deficiency of proapoptotic regulators Bim and Fas results in the early onset of systemic autoimmunity. *Immunity* 28, 206–217 (2008). [PubMed: 18275831]
72. Davide FR et al. Convergent Antibody Responses to SARS-CoV-2 in Convalescent Individuals. *Nature*.
73. Cruz-Teran C et al. Challenges and opportunities for antiviral monoclonal antibodies as COVID-19 therapy. *Advanced Drug Delivery Reviews* (2020).
74. Casadevall A & Pirofski L-a. The convalescent sera option for containing COVID-19. *The Journal of clinical investigation* 130 (2020).
75. Chen P et al. SARS-CoV-2 neutralizing antibody LY-CoV555 in outpatients with Covid-19. *New England Journal of Medicine* (2020).
76. Schäfer A et al. Antibody potency, effector function, and combinations in protection and therapy for SARS-CoV-2 infection in vivo. *Journal of Experimental Medicine* 218 (2020).
77. Group RC Dexamethasone in hospitalized patients with Covid-19—preliminary report. *New England Journal of Medicine* (2020).
78. Ware LB Physiological and biological heterogeneity in COVID-19-associated acute respiratory distress syndrome. *The Lancet Respiratory Medicine* (2020).
79. Singanayagam A et al. Duration of infectiousness and correlation with RT-PCR cycle threshold values in cases of COVID-19, England, January to May 2020. *Euro Surveill* 25, doi:10.2807/1560-7917.ES.2020.25.32.2001483 (2020).
80. Arons MM et al. Presymptomatic SARS-CoV-2 Infections and Transmission in a Skilled Nursing Facility. *N Engl J Med* 382, 2081–2090, doi:10.1056/NEJMoa2008457 (2020). [PubMed: 32329971]
81. Basile K et al. Cell-based culture of SARS-CoV-2 informs infectivity and safe de-isolation assessments during COVID-19. *Clin Infect Dis*, doi:10.1093/cid/ciaa1579 (2020).
82. Decker A et al. Prolonged SARS-CoV-2 shedding and mild course of COVID-19 in a patient after recent heart transplantation. *Am J Transplant* 20, 3239–3245, doi:10.1111/ajt.16133 (2020). [PubMed: 32519406]
83. Folgueira MD, Luczkowiak J, Lasala F, Pérez-Rivilla A & Delgado R Persistent SARS-CoV-2 replication in severe COVID-19. medRxiv, 2020.2006.2010.20127837, doi:10.1101/2020.06.10.20127837 (2020).
84. Jeong HW et al. Viable SARS-CoV-2 in various specimens from COVID-19 patients. *Clin Microbiol Infect* 26, 1520–1524, doi:10.1016/j.cmi.2020.07.020 (2020). [PubMed: 32711057]
85. Liu WD et al. Prolonged virus shedding even after seroconversion in a patient with COVID-19. *J Infect* 81, 318–356, doi:10.1016/j.jinf.2020.03.063 (2020).
86. van Kampen JJA et al. Duration and key determinants of infectious virus shedding in hospitalized patients with coronavirus disease-2019 (COVID-19). *Nat Commun* 12, 267, doi:10.1038/s41467-020-20568-4 (2021). [PubMed: 33431879]
87. Bussani R et al. Persistence of viral RNA, pneumocyte syncytia and thrombosis are hallmarks of advanced COVID-19 pathology. *EBioMedicine* 61, 103104 (2020). [PubMed: 33158808]

88. Yu H et al. A novel humanized mouse model with significant improvement of class-switched, antigen-specific antibody production. *Blood* 129, 959–969, doi:10.1182/blood-2016-04-709584 (2017). [PubMed: 28077418]
89. Wei J et al. Genome-wide CRISPR screens reveal host factors critical for SARS-CoV-2 infection. *Cell* (2020).
90. Sun F, Xiao G & Qu Z Murine bronchoalveolar lavage. *Bio-protocol* 7, e2287 (2017). [PubMed: 29082285]
91. Stuart T et al. Comprehensive integration of single-cell data. *Cell* 177, 1888–1902. e1821 (2019). [PubMed: 31178118]

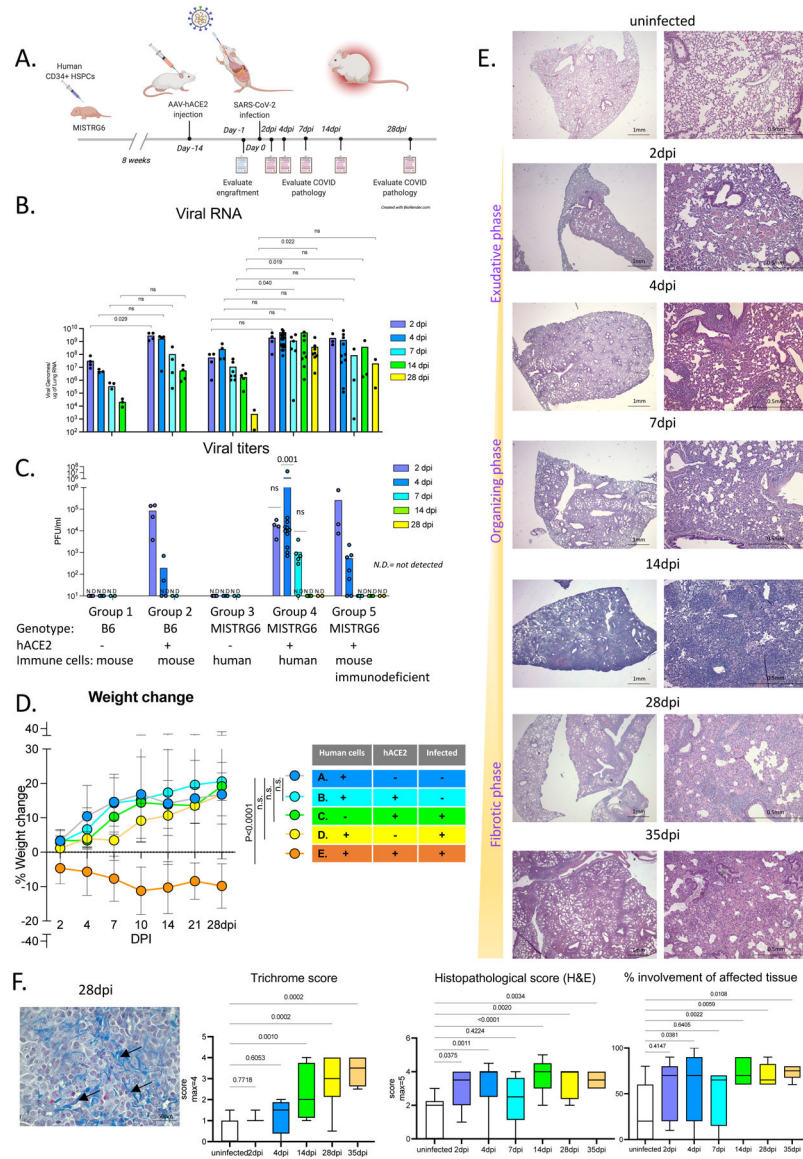


**Figure 1. MISTRG6 humanized mice that transiently express hACE2 can be infected with SARS-CoV-2.**

**A.** Schematic of experimental design. MISTRG6 mice were neonatally reconstituted with human CD34+ cells. After confirmation of human immune cell humanization in circulation, reconstituted MISTRG6 mice were injected with AAV-hACE2 (10<sup>11</sup> genomic copies/ml) intratracheally (MISTRG6-hACE2). Following a two-week acclimation and recovery period, MISTRG6-hACE2 mice were infected intranasally with SARS-CoV-2 (10<sup>6</sup> PFU).

**B.** Viral RNA (quantification of N gene) **C.** Viral titers measured by PFU in homogenized lung tissue at 2, 4, 7, 14, 28 days post-infection (dpi) in B6 control or reconstituted or unengrafted MISTRG6 mice expressing or lacking human ACE2 (using standard Vero E6 cells). Group 1: n=4(2dpi), 3(4dpi), 3(7dpi), 3(14dpi), 3(28dpi) biologically independent mice examined over 2 independent experiments. Group 2: n=4(2–28dpi) biologically independent mice examined over 2 independent experiments. Group 3: n=4(2dpi), 4(4dpi), 7(7dpi), 4(14dpi), 2(28dpi) biologically independent mice examined



over 3 independent experiments. Group 4: n=(2dpi), 26(4dpi), 6(7dpi), 8(14dpi), 8(28dpi) biologically independent mice examined over at least 4 independent experiments. Group 5: n=3(2dpi), 11(4dpi), 3(7dpi), 3(14dpi), 2(28dpi) biologically independent mice examined over at least 2 independent experiments; Significance in viral RNA was determined by Mann-Whitney, two-tailed test. One-sample t and Wilcoxon test was utilized for comparison of viral titers. Individual values for each mouse and means are presented.

**D.** Weight change during the course of infection plotted as percent change compared with original weight measured just before inoculation with SARS-CoV-2. Group A-D: N=7, Group E: N= 8 biologically independent mice examined over at least 3 independent experiments for 28 days. Means with SD experiments are presented. Ordinary one-way ANOVA compared to the mean of uninfected reconstituted MISTRG6 mice (Group A) with Dunnett's multiple comparison test was utilized. Group E p-value <0.0001; Group D p-value= 0.2889; Group C p-value= 0.8926, Group B p-value=0.9974. Means with SD are plotted. Individual values for Group E are presented in Fig S1C.

**E.** Representative images of H&E staining (2x and 10x magnification) and box and whisker plot (min to max) of the histopathological scores and percent area affected of infected (2, 4, 7, 14, 28 and 35dpi) or uninfected lungs. The whiskers go down to the smallest value (min) and up to the largest (max). The box extends from the 25th to 75th percentiles. The median is shown as a line in the center of the box. Uninfected n=9, 2dpi n=5, 4dpi n=14, 7dpi n=6, 14dpi n=11, 28dpi n=10, 35dpi n=6 biologically independent mice examined over at least 3 independent experiments. Ordinary one-way ANOVA compared to uninfected lungs was utilized. P value was adjusted by Šídák's multiple comparisons test.

**F.** Trichrome staining of infected (2, 4, 7, 14, 28 and 35dpi) or uninfected lungs. Representative images (40X) and box and whisker plot (min to max) of the histopathological scores are presented. Arrows indicate areas with Collagen deposition. The extend of fibrosis was determined by the thickness of collagen bundles. The whiskers go down to the smallest value (min) and up to the largest (max). The box extends from the 25th to 75th percentiles. The median is shown as a line in the center of the box. Uninfected n=7, 2dpi n=3, 4dpi n=4, 14dpi n=12, 28dpi n=8, 35dpi n=4 biologically independent mice examined over at least 3 independent experiments. Ordinary one-way ANOVA compared to uninfected lungs was utilized. P value was adjusted by Šídák's multiple comparisons test. Representative images of all time points are presented as part of Fig S1F.

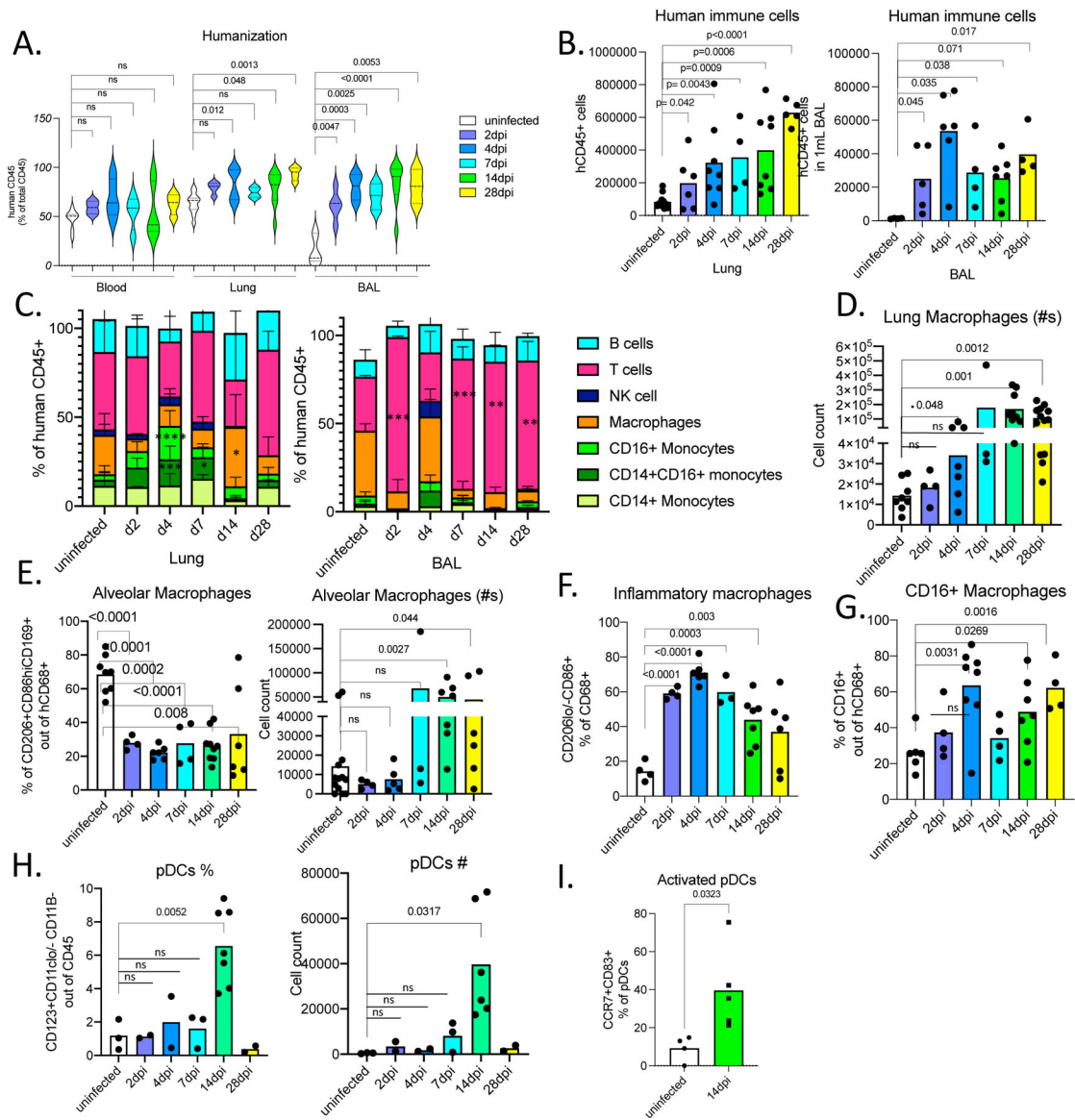


**Figure 2. Immune landscape in MISTRG6-hACE2 mice infected with SARS-CoV-2 is characterized by inflammatory macrophages and monocytes.**

**A.** Humanization measured by ratio of human CD45+ (human immune cells) cells in total CD45+ cells (mouse and human CD45+ combined) in blood, lungs, and BAL of uninfected and infected MISTRG6-hACE2 mice. Uninfected n=8, 2dpi n=4, 4dpi n=7, 7dpi n=4, 14dpi n=9, 28dpi n=4 biologically independent mice examined over at least 3 independent experiments. Ordinary one-way ANOVA compared to uninfected lungs was utilized. P value was adjusted with Dunnett's multiple comparison test. Distribution of individual data points is displayed in a violin plot.

**B.** Human immune cell numbers in lungs and BAL of uninfected and infected mice at 2,4,7,14,28 dpi. Lung: Uninfected n=11, 2dpi n=6, 4dpi n=7, 7dpi n=4, 14dpi n=8, 28dpi n=5 over at least 3 independent experiments. BAL: Uninfected n=4, 2dpi n=5, 4dpi n=6, 7dpi n=4, 14dpi n=7, 28dpi n=4 over at least 3 independent experiments. Unpaired, two-

tailed t-test. P values <0.05 are plotted. Individual values for each mouse and means are presented.

**C.** Human immune lineages lungs and BAL of uninfected and infected mice at 2,4,7,14, 28 dpi within the human CD45+ population. Classical monocytes (CD14+), Intermediate monocytes (CD14+CD16+), non-classical monocytes (CD16+CD14-), macrophages (CD68+), NK cells (NKP46+), T cells (CD3+), B cells (CD19+ and/or CD20+). Statistical significance was deemed by ordinary one-way ANOVA compared to uninfected lungs. P values were adjusted with Dunnett's multiple comparison test. P values represented by: ns P > 0.05; \*P 0.05; \*\*P 0.01; \*\*\*P 0.001; \*\*\*\*P 0.0001. Lung: Uninfected n=8, 2dpi n=4, 4dpi n=7, 7dpi n=3, 14dpi n=9, 28dpi n=5 biologically independent mice examined over at least 3 independent experiments. BAL: Uninfected n=4, 2dpi n=4, 4dpi n=6, 7dpi n=3, 14dpi n=6, 28dpi n=3 biologically independent mice examined over at least 3 independent experiments. P values <0.05 are provided: Lung: CD14+CD16+ monocytes 4dpi=0.0003, 7dpi =0.030; CD16+ monocytes 4dpi<0.0001; Macrophages 14dpi= 0.0114. BAL: T cells 2dpi<0.0001, 7dpi=0.0003, 14dpi=0.003, 28dpi=0.001; Means with SD are plotted.

**D.** Number of human macrophages in lungs of uninfected and infected mice at 2, 4, 7, 14, 28 dpi. Unpaired, two-tailed t-test. Lung: Uninfected n=8, 2dpi n=4, 4dpi n=7, 7dpi n=3, 14dpi n=9, 28dpi n=6 biologically independent mice examined over at least 3 independent experiments. Individual values for each mouse and means are presented.

**E.** Frequency and number of human alveolar macrophages marked by CD206hi, CD86+, CD169+ expression within the hCD45+CD68+ population in the lungs of uninfected and infected mice at 2, 4, 7, 14, 28 dpi. N=3–10. Unpaired, two-tailed t-test. Uninfected n=8, 2dpi n=4, 4dpi n=4–6, 7dpi n=3, 14dpi n=7, 28dpi n=6 biologically independent mice examined over at least 3 independent experiments. Individual values for each mouse and means are presented.

**F.** Frequency of inflammatory human lung macrophages marked by CD206-/lo, CD86hi macrophages within the hCD45+CD68+ population in the lungs of uninfected and infected mice at 2,4,7,14,28 dpi. Unpaired, two-tailed t-test. P values<0.05 plotted. Uninfected n=4, 2dpi n=4, 4dpi n=6, 7dpi n=4, 14dpi n=7, 28dpi n=4 biologically independent mice examined over 3 independent experiments. Individual values for each mouse and means are presented.

**G.** Frequency of CD16+ human lung macrophages marked by CD16+ cells within the hCD45+CD68+ population in the lungs of uninfected and infected mice at 2,4,7,14,28 dpi. N=4–8. Unpaired, two-tailed t-test. P values<0.05 plotted. Uninfected n=6, 2dpi n=4, 4dpi n=8, 7dpi n=3, 14dpi n=7, 28dpi n=6 biologically independent mice examined over 3 independent experiments. Individual values for each mouse and means are presented. Unpaired t-test, two-tailed. P values <0.05 are plotted.

**H.** Frequency and number of human plasmacytoid dendritic cells (pDCs) marked by CD123+CD11b-CD11c-/lo cells within hCD45+ population in the lungs of uninfected and infected mice at 2,4,7,14,28 dpi. Unpaired t-test, two-tailed. Uninfected n=3, 2dpi n=2, 4dpi n=2, 7dpi n=3, 14dpi n=7, 28dpi n=2 biologically independent mice examined over at least 2 independent experiments. Individual values for each mouse and means are presented.

**I.** Frequencies of activated, mature (CD83+ CCR7+) pDCs in infected lungs at 14dpi or uninfected lungs.

Uninfected n=4, 14dpi n=5 biologically independent mice examined over 2 independent experiments. Individual values for each mouse and means are presented. Unpaired t-test, two-tailed. P values <0.05 are plotted.

Author Manuscript

Author Manuscript

Author Manuscript

Author Manuscript

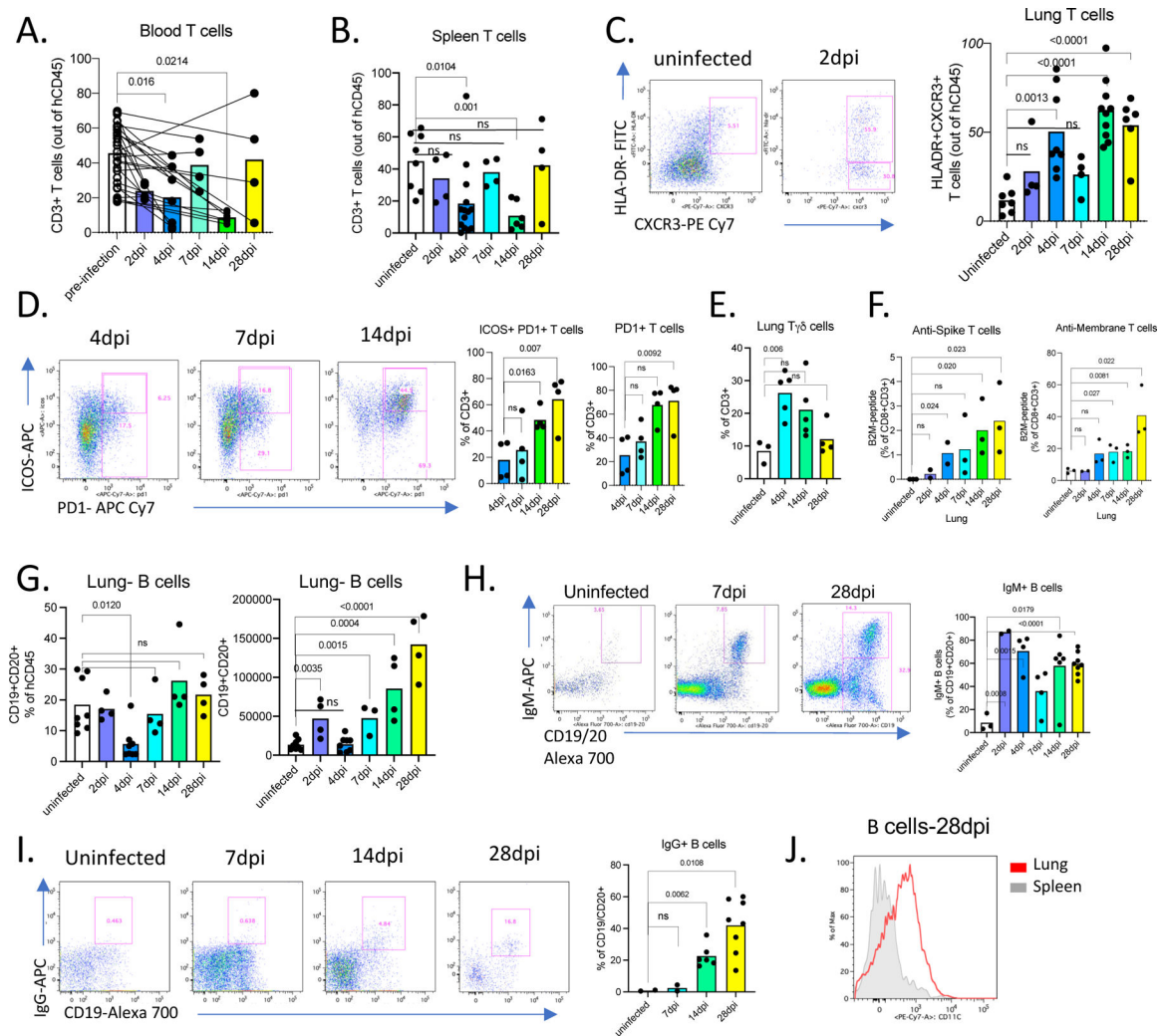


**Figure 3. Adaptive immune responses in MISTRG6-hACE2 mice infected with SARS-CoV-2 are characterized by virus specific, activated T cells, IgG+ B cells and systemic lymphopenia.**

**A.** Frequencies of human CD3+ T cells within human CD45+ population in the blood pre- and post-infection (2,4,7,14,28dpi). Lines connect pre- and post-infection values for the same mouse. Paired, two-tailed t-test. 2dpi n=4, 4dpi n=7, 7dpi n=4, 14dpi n=6, 28dpi n=4 biologically independent mice examined over 3 independent experiments. Individual values for each mouse and means are presented. P-values<0.05 are plotted.

**B.** Frequencies of human CD3+ T cells within human CD45+ population in the spleens of uninfected and infected mice at 2,4,7,14,28 dpi. Uninfected n=8, 2dpi n=4, 4dpi n=14, 7dpi n=4, 14dpi n=6, 28dpi n=4 biologically independent mice examined over at least 3 independent experiments. Unpaired, two-tailed t-test. Individual values for each mouse and means are presented. P-values<0.05 are plotted.

**C.** Representative flow cytometry plots of HLA-DR and CXCR3 expression on human lung T cells and frequencies of HLA-DR+CXCR3+ lung T cells in uninfected and infected mice at 2,4,7,14,28dpi. Uninfected n=7, 2dpi n=4, 4dpi n=8, 7dpi n=4, 14dpi n=9, 28dpi n=6 biologically independent mice examined over at least 3 independent experiments. Unpaired,

two-tailed t-test. Individual values for each mouse and means are presented. P-values<0.05 are plotted.

**D.** Representative flow cytometry plots of ICOS and PD1 expression on human lung T cells and frequencies Icos+ PD1+ or PD1+ T cells in uninfected and infected mice (4,7,14,28dpi). N=4 biologically independent mice examined over at least 3 independent experiments. Unpaired, two-tailed t-test. Individual values for each mouse and means are presented. P-values<0.05 are plotted.

**E.** Frequencies of TCRgamma/delta T cells ( $T\gamma\delta$ ) among human lung T cells in uninfected and infected mice (4,14,28dpi). Uninfected n=3, 4dpi n=5, 14dpi n=5, 28dpi n=4 biologically independent mice examined over at least 3 independent experiments. Unpaired, two-tailed t-test. Individual values for each mouse and means are plotted. P-values<0.05 are plotted.

**F.** Frequencies of anti-viral CD8+ T cells in uninfected and infected mice at 2,4,7,14,28dpi. Human CD8+ T cells from mice that had been engrafted with an HLA-A2 positive source of progenitor cells were stained with viral antigen (peptides of M and S viral proteins)-bearing HLA-A2 tetramers. Uninfected n=3, 2dpi n=2, 4dpi n=3, 7dpi n=3, 14dpi n=3, 28dpi n=3 biologically independent mice examined over 2 independent experiments. Unpaired, two-tailed t-test. Individual values for each mouse and means are presented. P-values<0.05 are plotted.

**G.** Frequencies and numbers of human B cells within hCD45+ population in the lungs of uninfected or infected mice at 2,4,7,14,28 dpi. Uninfected n=8, 2dpi n=4, 4dpi n=8, 7dpi n=4, 14dpi n=4, 28dpi n=4 biologically independent mice examined over at least 2 independent experiments. Unpaired, two-tailed t-test. Individual values for each mouse and means are presented. P-values<0.05 are plotted.

**H.** Representative flow cytometry plots and frequencies of IgM+ B cells in the lungs of uninfected and infected mice 2,4,7,14,28dpi. N=3–8. Unpaired, two-tailed t-test. P-values<0.05 are plotted. Uninfected n=3, 2dpi n=2, 4dpi n=4, 7dpi n=4, 14dpi n=6, 28dpi n=8 biologically independent mice examined over at least 2 independent experiments. Unpaired, two-tailed t-test. Individual values for each mouse and means are presented. P-values<0.05 are plotted.

**I.** Representative flow cytometry plots and frequencies of IgG+ B cells in the lungs of uninfected and infected mice 7,14,28dpi. N=2–8. Unpaired, two-tailed t-test. P-values<0.05 are plotted. Uninfected n=2, 7dpi n=2, 14dpi n=6, 28dpi n=8 biologically independent mice examined over at least 2 independent experiments. Unpaired, two-tailed t-test. Individual values for each mouse and means are presented. P-values<0.05 are plotted.

**J.** Representative plot of CD11c expression on CD19+ B cells from spleen and lungs of infected mice at 28dpi. N=5. Representative of n=6 for at least 3 independent experiments. All attempts resulted with similar findings.

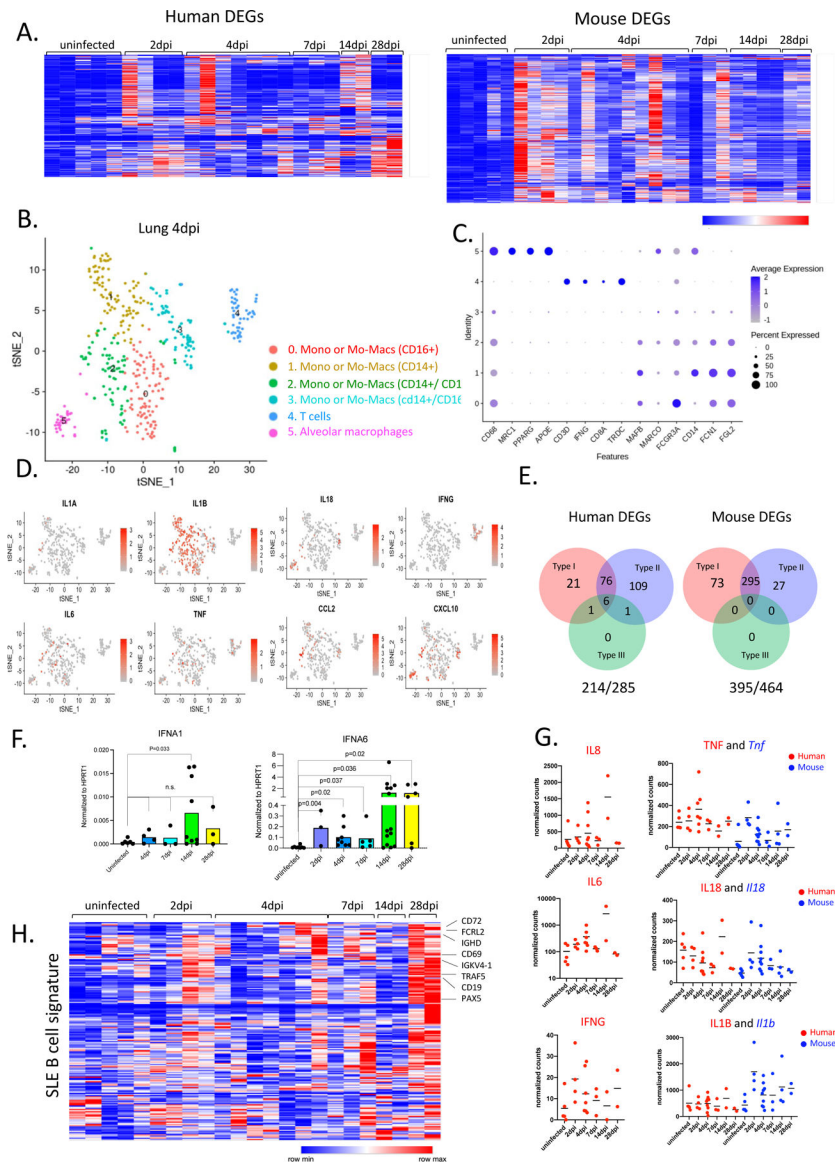


**Figure 4. SARS-CoV-2 lungs sustain ISGs and display SLE like features**

**A.** Heatmap of differentially regulated human and mouse genes (combined list of genes Log<sub>2</sub> FoldChange >1 in each infected time point vs uninfected lungs; adjusted p value < 0.05; mean normalized count > 5). Transformed normalized counts in lungs of uninfected or infected MISTRG6-hACE2 plotted over the course of infection were clustered using Spearman Correlation. Row min and max of transformed values, calculated by subtracting row mean and dividing by STD for each gene across all samples, are visualized. For the adjusted P values the Bonferroni correction was used. Human genes: Uninfected n=5, 2dpi n=4, 4dpi n=7, 7dpi n=3, 14dpi n=2, 28dpi n=2 biologically independent mice examined over at least 2 independent experiments for all time points. Mouse genes: Uninfected n=5, 2dpi n=4, 4dpi n=9, 7dpi n=3, 14dpi n=4, 28dpi n=2 biologically independent mice examined over at least 2 independent experiments for all time points.

Whole tissue lung samples with less than 1% human reads were excluded from analysis (pre-established criterium).

**B.** t-distributed stochastic neighbor embedding (*t*-SNE) plot with clustering results of single cell RNA sequencing of human immune cells using the 10X Genomics platform from lungs at 4dpi. Single cell suspensions from whole infected lung at 4dpi were processed and sequenced. There were 421 cells identified as human immune cells.

**C.** Dot plot of cluster identifying genes for human immune cell clusters described in Fig. 4B.

**D.** Cluster distribution and expression profile of human inflammatory cytokines for clusters described in Fig. 4B–C.

**E.** Distribution of ISGs within human and mouse DEGs.

**F.** Normalized expression of human IFNA1 and IFNA6 mRNA measured by qPCR in homogenized lung tissue of uninfected and infected (2, 4, 7, 14, 28dpi) mice. Expression was normalized to human HPRT1. Unpaired t-test, one-tailed since the distribution is expected to be one-sided. Uninfected n=6, 4dpi n=4, 7dpi n=3, 14dpi n=9, 28dpi n=3 biologically independent mice examined over at least 3 independent experiments. Individual values for each mouse and means are presented. P-values<0.05 are plotted.

**G.** Normalized counts for inflammatory cytokines implicated in COVID-19 patients. Counts were reported separately for human(red) and mouse(blue) cytokine genes. Based on whole tissue transcriptome data presented in Fig. 4A. Human genes: Uninfected n=5, 2dpi n=4, 4dpi n=7, 7dpi n=3, 14dpi n=2, 28dpi n=2 biologically independent mice examined over at least 2 independent experiments for all time points. Mouse genes: Uninfected n=5, 2dpi n=4, 4dpi n=9, 7dpi n=3, 14dpi n=4, 28dpi n=2 biologically independent mice examined over at least 2 independent experiments for all time points.

**H.** Heatmap of genes that are implicated in SLE-like B cells based on GSE10325<sup>71</sup> in infected lungs of MISTRG6 mice at 2,4,7,14,28 dpi. Row min and max of transformed values, calculated by subtracting row mean and diving by STD for each gene across all samples, are visualized. Uninfected n=5, 2dpi n=4, 4dpi n=7, 7dpi n=3, 14dpi n=2, 28dpi n=2 biologically independent mice examined over at least 2 independent experiments for all time points.



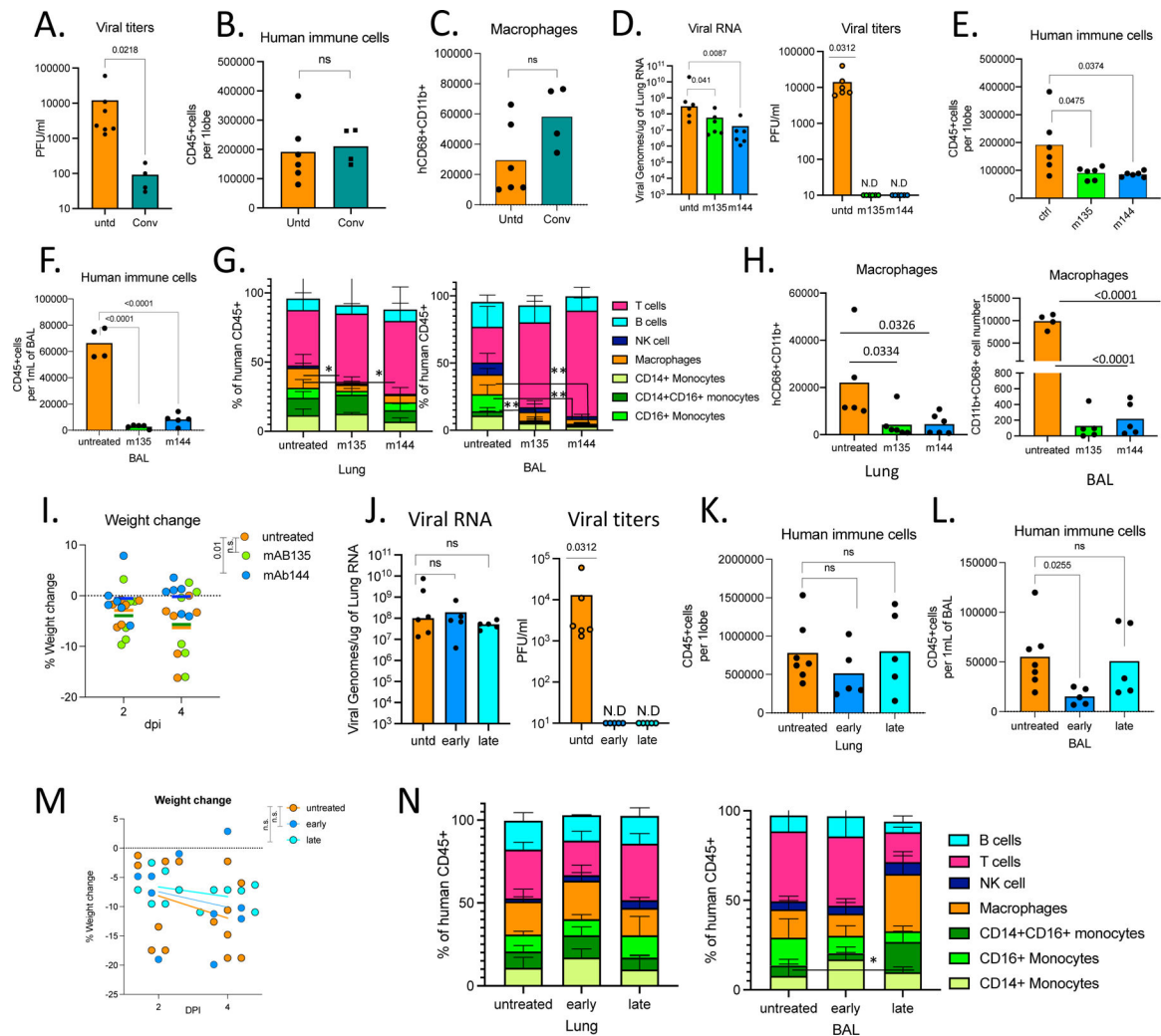


**Figure 5. Human monoclonal recombinant antibodies as prophylactic and therapeutic interventions impact disease outcome.**

**A.** Viral titers measured by PFU in homogenized lung tissue at 4 dpi in MISTRG6-hACE2 mice that received prophylactic treatment of convalescent patient plasma or left untreated. Paired, two-tailed t-test. Untreated controls: n=6, convalescent treated group n=4 biologically independent mice examined over 2 independent experiments. Individual values for each mouse and means are presented.

**B.** Human immune cells at 4 dpi in lungs of MISTRG6-hACE2 mice that received prophylactic treatment of convalescent patient serum or left untreated. Paired, two-tailed t-test. Untreated controls: n=6, convalescent treated group n=4 biologically independent mice examined over 2 independent experiments. Individual values for each mouse and means are presented.

**C.** Human macrophages (hCD45+ hCD68+) at 4 dpi in lungs of MISTRG6-hACE2 mice that received prophylactic treatment of convalescent patient serum or left untreated. Paired, two-tailed t-test. Untreated controls: n=6, convalescent treated group n=4 biologically independent mice examined over 2 independent experiments. Individual values for each mouse and means are presented.

**D.** Viral RNA and viral titers measured by PFU in homogenized lung tissue at 4 dpi in MISTRG6-hACE2 mice that received prophylactic treatment of monoclonal antibody clone 135 (m135) or clone 144(m144) 8 hours prior to infection or left untreated (untd). N=6. Mann-Whitney, two-tailed test was used for comparison of viral RNA. One-sample Wilcoxon signed rank test was used to determine significance in the viral titer quantification (effect size=0.9, W=21).

**E.** Human immune cells in lungs of MISTRG6-hACE2 mice received a prophylactic treatment of monoclonal antibody clone 135 (m135) or clone 144(m144) 8 hours prior to infection or left untreated (untd). N=6 biologically independent mice examined over 2 independent experiments. Individual values for each mouse and means are presented. Unpaired t-test, two-tailed.

**F.** Human immune cells in BAL of MISTRG6-hACE2 mice received a prophylactic treatment of monoclonal antibody clone 135 (m135) or clone 144(m144) 8 hours prior to infection or left untreated (untd). Untreated control n=4, treated group n=5 biologically independent mice examined over 2 independent experiments. Individual values for each mouse and means are presented. Unpaired t-test, two-tailed.

**G.** Human immune lineages lungs and BAL of mAb treated or untreated mice at 4 dpi within the human CD45+ population. Classical monocytes (CD14+), Intermediate monocytes (CD14+CD16), non-classical monocytes (CD16+CD14-), macrophages (CD68+), NK cells (NKP46+), T cells (CD3+), B cells (CD19+ and/or CD20+). MISTRG6-hACE2 mice received a prophylactic treatment of monoclonal antibody clone 135 (m135) or clone 144(m144) 8 hours prior to infection or left untreated (untd). In lungs, N=6 biologically independent mice examined over 3 independent experiments. Individual values for each mouse and means are presented. In BAL, Untreated control N=4, treated group n=5 biologically independent mice examined over 2 independent experiments. Individual values for each mouse and means are presented. Unpaired t-test, two-tailed. Statistical significance was deemed by comparison to uninfected group. P values represented by: ns P > 0.05; \*P 0.05; \*\*P 0.01; \*\*\*P 0.001; \*\*\*\*P 0.0001. Only changes in frequencies of lung macrophages (m135 p value=0.029, m144 p value =0.037) and BAL macrophages (m144 p value =0.0042) and monocytes (CD16+ (m135 p value=0.0051, m144 p value=0.0058) were statistically significant.

**H.** Human macrophages (hCD45+ hCD68+) at 4 dpi in lungs and BAL of MISTRG6-hACE2 mice that received prophylactic treatment of mAbs (clone 135 or 144) or left untreated. Lungs: Untreated control N=6, treated group n=5 biologically independent mice examined over 3 independent experiments. BAL: Untreated control N=5, treated group n=4 biologically independent mice examined over 2 independent experiments. Individual values for each mouse and means are presented. Unpaired t-test, two-tailed.

**I.** Weight change in mAb treated mice (prophylaxis) at 2 and 4dpi plotted as percent change compared with original weight measured just before inoculation with SARS-CoV-2. N=6 biologically independent mice examined over 2 independent experiments. RM-one-way ANOVA with Dunnett's multiple comparison test comparing weight change at 4dpi to untreated group was utilized. P-value for m144=0.01, p-value for m135=0.98. Individual values for each mouse and means are presented.

**J.** Viral RNA and viral titers measured by PFU in homogenized lung tissue at 4 dpi in MISTRG6-hACE2 mice that received post-infection treatment of a mixed cocktail of

monoclonal antibodies clone 135 (m135) and clone 144(m144) or left untreated (untd). Early treatment groups were treated 11 hours post-infection and late treatment 35 hours post-infection. Mann-Whitney, two-tailed test was used for comparison of viral RNA. One-sample Wilcoxon signed rank test was used to determine significance in the viral titer quantification (effect size=0.9, W=21). Untreated control N=6, early and late treated groups n=5 biologically independent mice examined over 3 independent experiments. Individual values for each mouse and means are presented.

**K.** Human immune cells in lungs of MISTRG6-hACE2 mice that received early, late or no treatment of monoclonal antibody mix. Untreated control N=6, early and late treated groups n=5 biologically independent mice examined over 3 independent experiments. Individual values for each mouse and means are presented.

Unpaired, two-tailed t-test. P-values<0.05 are plotted.

**L.** Human immune cells in BAL of MISTRG6-hACE2 mice that received early, late or no treatment of monoclonal antibody mix. Untreated control N=4, early and late treated groups n=5 biologically independent mice examined over 3 independent experiments. Individual values for each mouse and means are presented.

Unpaired, two-tailed t-test. P-values<0.05 are plotted. Untreated control N=6, early and late treated groups n=5 biologically independent mice examined over 3 independent experiments. Individual values for each mouse and means are presented.

**M.** Weight change upon mAb therapeutic treatment at days and days post-infection plotted as percent change compared with original weight measured just before inoculation with SARS-Cov-2. N=6 biologically independent mice examined over 3 independent experiments. Individual values for each mouse and means are presented. One-way ANOVA (Šídák's multiple comparisons test) comparing weight change at 4dpi to untreated group was utilized. Early treatment vs untreated p value=0.8 and late treatment vs untreated p value=0.49.

**N.** Human immune lineages lungs and BAL of mAb treated or untreated mice at 4 dpi within the human CD45+ population. Classical monocytes (CD14+), Intermediate monocytes (CD14+CD16), non-classical monocytes (CD16+CD14-), macrophages (CD68+), NK cells (NKP46+), T cells (CD3+), B cells (CD19+ and/or CD20+). MISTRG6-hACE2 mice received a prophylactic treatment of monoclonal antibody clone 135 (m135) or clone 144(m144) 8 hours prior to infection or left untreated (untd). Lung: untreated control N=6, early and late treated groups n=5 biologically independent mice examined over 3 independent experiments. Individual values for each mouse and means are presented. BAL: Untreated control N=4, early and late treated groups n=5 biologically independent mice examined over 3 independent experiments. Individual values for each mouse and means are presented. Statistical significance was deemed by unpaired t-test compared to uninfected group. P values represented by: ns P > 0.05; \*P 0.05; \*\*P 0.01; \*\*\*P 0.001; \*\*\*\*P 0.0001. Only changes in frequencies of monocytes (CD14+CD16+) were statistically significant (p value=0.01). Means with SD are plotted.

In Figure 5, MISTRG6 mice were engrafted with CD34+ cells neonatally isolated from at least 2 donors. Pooled or infection matched representative results of at least 2 independent experiments are presented. Only P-values <0.05 are shown. Mean with SD or individual values are plotted.

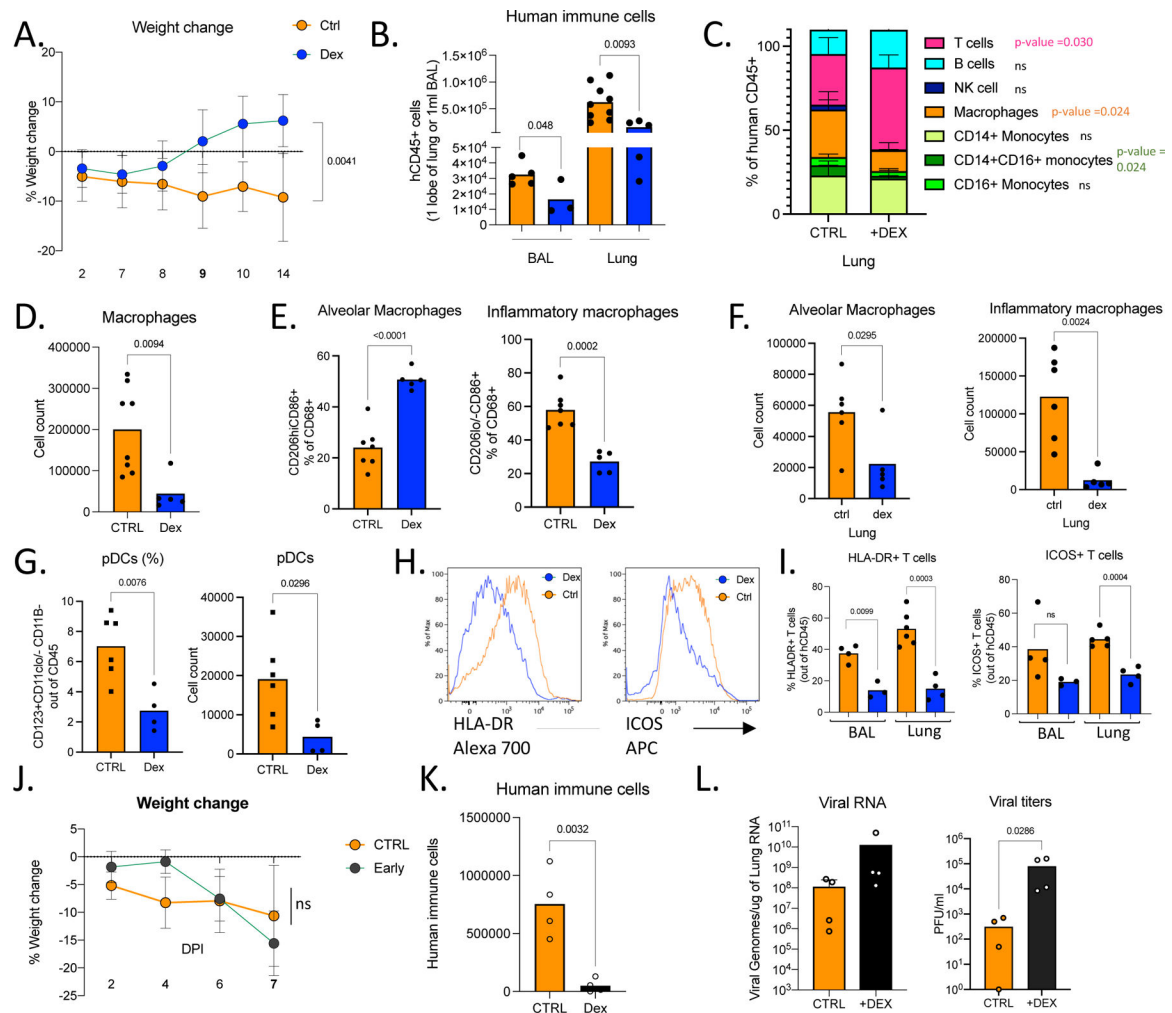


**Figure 6. Accurate timing of corticosteroids is necessary to balance viral clearance and prevent immunopathology.**

**A.** Weight change in dexamethasone treated or control mice during SARS-CoV-2 infection plotted as percent change compared with original weight prior to viral inoculation. Mice were treated with dexamethasone at 7,8,9 dpi. Untreated n=8, treated n=6 biologically independent mice examined over 3 independent experiments. Unpaired, two-tailed t-test determined comparing 14dpi values (p=0.0041). Means with SD are plotted.

**B.** Human immune cells in 14dpi lungs and BAL of MISTRG6-hACE2 mice treated with dexamethasone at 7, 8 9 dpi or left untreated. Untreated n=8, treated n=6 biologically independent mice examined over 3 independent experiments. Unpaired, two-tailed t-test. Individual values for each mouse and means are plotted.

**C.** Human immune lineages lungs of dexamethasone treated or untreated mice within the human CD45+ population. Classical monocytes (CD14+), Intermediate monocytes (CD14+CD16), non-classical monocytes (CD16+CD14-), macrophages (CD68+), NK cells (NKP46+), T cells (CD3+), B cells (CD19+ and/or CD20+). MISTRG6-hACE2 mice were treated with dexamethasone at 7,8,9dpi. N=4–6. Unpaired, two-tailed t-test. Untreated n=6, treated n=5 biologically independent mice examined over 3 independent experiments. Means with SD are plotted.

**D.** Number of human macrophages in lungs of dexamethasone treated and untreated mice at 14dpi. N=6. Unpaired, two-tailed t-test. Untreated n=8, treated n=5 biologically independent mice examined over 3 independent experiments. Individual values for each mouse and means are plotted.

**E.** Frequencies of alveolar or inflammatory macrophages in the lungs of MISTRG6-hACE2 mice that were treated with dexamethasone or left untreated. N=6. Unpaired, two-tailed t-test. Untreated n=7, treated n=5 biologically independent mice examined over 3 independent experiments. Individual values for each mouse and means are plotted.

**F.** Numbers of alveolar or inflammatory macrophages in the lungs of MISTRG6-hACE2 mice that were treated with dexamethasone or left untreated. N=6. Unpaired, two-tailed t-test. Untreated n=6, treated n=5 biologically independent mice examined over 3 independent experiments. Individual values for each mouse and means are plotted.

**G.** Frequencies (left) and numbers (right) of pDCs at 14dpi in the lungs of dexamethasone treated or control mice. N=6. Unpaired, two-tailed t-test. Untreated n=5, treated n=4 biologically independent mice examined over 3 independent experiments. Individual values for each mouse and means are plotted.

**H.** Representative histograms for HLA-DR expression in lung T cells at 14dpi in dexamethasone treated or control mice. N=6. Unpaired, two-tailed t-test. Representative of n=4 for examined over 2 independent experiments. All attempts resulted with similar findings.

**I.** Frequencies of HLA-DR+ or ICOS+ T cells at 14dpi in the lungs and BAL of dexamethasone treated or control mice. N=4–6. Unpaired, two-tailed t-test. Lung: untreated n=5, treated n=4 biologically independent mice examined over 3 independent experiments. BAL: untreated n=4, treated n=3 biologically independent mice examined over 3 independent experiments. Individual values for each mouse and means are plotted.

**J.** Weight change in dexamethasone treated or control mice during SARS-CoV-2 infection plotted as percent change compared with original weight prior to viral inoculation. Mice were treated with dexamethasone at 3,4,5dpi. Untreated n=6, treated n=4 biologically independent mice examined over 2 independent experiments. Unpaired, two-tailed t-test. Means with SD are plotted.

**K.** Human immune cells in lungs of MISTRG6-hACE2 mice treated with dexamethasone at 3, 4 5 dpi or left untreated (ctrl). N= 4 biologically independent mice examined over 2 independent experiments. Unpaired, two-tailed t-test. Individual values for each mouse and means are plotted

**L.** Viral RNA and viral titers measured by PFU in homogenized lung tissue at 7 dpi in dexamethasone treated or control mice. N= 4 biologically independent mice examined over 2 independent experiments. Unpaired, two-tailed t-test. Individual values for each mouse and means are plotted. Mann-Whitney test, two-tailed.

MISTRG6 mice were engrafted with CD34+ cells neonatally isolated from at least 2 donors. Pooled or infection matched representative results of at least 2 independent experiments are presented. Only P-values <0.05 are plotted. Mean with SD or individual values are plotted.